

PAPER

## QUBIC VI: Cryogenic half wave plate rotator, design and performance

To cite this article: The QUBIC collaboration *et al* JCAP04(2022)039

View the [article online](#) for updates and enhancements.

### You may also like

- [QUBIC I: Overview and science program](#)  
The QUBIC collaboration, J.-Ch. Hamilton,  
L. Mousset et al.
- [An integrated programming and  
development environment for adiabatic  
quantum optimization](#)  
T S Humble, A J McCaskey, R S Bennink  
et al.
- [QUBIC VII: The feedhorn-switch system of  
the technological demonstrator](#)  
The QUBIC collaboration, F. Cavaliere, A.  
Mennella et al.



**IOP | ebooks™**

Bringing together innovative digital publishing with  
leading authors from the global scientific community.

Start exploring the collection—download the  
first chapter of every title for free.

# QUBIC VI: Cryogenic half wave plate rotator, design and performance



## The QUBIC collaboration

G. D'Alessandro,<sup>1,2,a</sup> L. Mele,<sup>1,2,a</sup> F. Columbro,<sup>1,2,a</sup> G. Amico,<sup>1</sup>  
E.S. Battistelli,<sup>1,2</sup> P. de Bernardis,<sup>1,2</sup> A. Coppolecchia,<sup>1,2</sup>  
M. De Petris,<sup>1,2</sup> L. Grandsire,<sup>3</sup> J.-Ch. Hamilton,<sup>3</sup> L. Lamagna,<sup>1,2</sup>  
S. Marnieros,<sup>4</sup> S. Masi,<sup>1,2</sup> A. Mennella,<sup>5,6</sup> C. O'Sullivan,<sup>7</sup>  
A. Paiella,<sup>1,2</sup> F. Piacentini,<sup>1,2</sup> M. Piat,<sup>3</sup> G. Pisano,<sup>8</sup> G. Presta,<sup>1,2</sup>  
A. Tartari,<sup>9</sup> S.A. Torchinsky,<sup>3,10</sup> F. Voisin,<sup>3</sup> M. Zannoni,<sup>11,12</sup>  
P. Ade,<sup>8</sup> J.G. Alberro,<sup>13</sup> A. Almela,<sup>14</sup> L.H. Arnaldi,<sup>15</sup> D. Auguste,<sup>4</sup>  
J. Aumont,<sup>16</sup> S. Azzoni,<sup>17</sup> S. Banfi,<sup>11,12</sup> A. Baù,<sup>11,12</sup> B. Bélier,<sup>18</sup>  
D. Bennett,<sup>7</sup> L. Bergé,<sup>4</sup> J.-Ph. Bernard,<sup>16</sup> M. Bersanelli,<sup>5,6</sup>  
M.-A. Bigot-Sazy,<sup>3</sup> J. Bonaparte,<sup>19</sup> J. Bonis,<sup>4</sup> E. Bunn,<sup>20</sup>  
D. Burke,<sup>7</sup> D. Buzi,<sup>1</sup> F. Cavaliere,<sup>5,6</sup> P. Chanial,<sup>3</sup> C. Chapron,<sup>3</sup>  
R. Charlassier,<sup>3</sup> A.C. Cobos Cerutti,<sup>14</sup> G. De Gasperis,<sup>21,22</sup>  
M. De Leo,<sup>1,23</sup> S. Dheilly,<sup>3</sup> C. Duca,<sup>14</sup> L. Dumoulin,<sup>4</sup>  
A. Etchegoyen,<sup>14</sup> A. Fasciszewski,<sup>19</sup> L.P. Ferreyro,<sup>14</sup> D. Fracchia,<sup>14</sup>  
C. Franceschet,<sup>5,6</sup> M.M. Gamboa Larena,<sup>24,33</sup> K.M. Ganga,<sup>3</sup>  
B. García,<sup>14</sup> M.E. García Redondo,<sup>14</sup> M. Gaspard,<sup>4</sup> D. Gayer,<sup>7</sup>  
M. Gervasi,<sup>11,12</sup> M. Giard,<sup>16</sup> V. Gilles,<sup>1</sup> Y. Giraud-Heraud,<sup>3</sup>  
M. Gómez Berisso,<sup>15</sup> M. González,<sup>15</sup> M. Gradziel,<sup>7</sup> M.R. Hampel,<sup>14</sup>  
D. Harari,<sup>15</sup> S. Henrot-Versillé,<sup>4</sup> F. Incardona,<sup>5,6</sup> E. Jules,<sup>4</sup>  
J. Kaplan,<sup>3</sup> C. Kristukat,<sup>25</sup> S. Loucatos,<sup>3,26</sup> T. Louis,<sup>4</sup> B. Maffei,<sup>27</sup>  
W. Marty,<sup>16</sup> A. Mattei,<sup>2</sup> A. May,<sup>28</sup> M. McCulloch,<sup>28</sup> D. Melo,<sup>14</sup>  
L. Montier,<sup>16</sup> L. Mousset,<sup>3</sup> L.M. Mundo,<sup>13</sup> J.A. Murphy,<sup>7</sup>  
J.D. Murphy,<sup>7</sup> F. Nati,<sup>11,12</sup> E. Olivieri,<sup>4</sup> C. Oriol,<sup>4</sup> F. Pajot,<sup>16</sup>

<sup>a</sup>Main author.

**A. Passerini,<sup>11,12</sup> H. Pastoriza,<sup>15</sup> A. Pelosi,<sup>2</sup> C. Perbost,<sup>3</sup>  
M. Perciballi,<sup>2</sup> F. Pezzotta,<sup>5,6</sup> L. Piccirillo,<sup>28</sup> M. Platino,<sup>14</sup>  
G. Polenta,<sup>29</sup> D. Prêle,<sup>3</sup> R. Puddu,<sup>30</sup> D. Rambaud,<sup>16</sup> E. Rasztocky,<sup>31</sup>  
P. Ringegni,<sup>13</sup> G.E. Romero,<sup>31</sup> J.M. Salum,<sup>14</sup> A. Schillaci,<sup>32</sup>  
C.G. Scóccola,<sup>24,33</sup> S. Scully,<sup>7,34</sup> S. Spinelli,<sup>11</sup> G. Stankowiak,<sup>3</sup>  
M. Stolpovskiy,<sup>3</sup> A.D. Supanitsky,<sup>14</sup> J.-P. Thermeau,<sup>3</sup> P. Timbie,<sup>35</sup>  
M. Tomasi,<sup>5,6</sup> C. Tucker,<sup>8</sup> G. Tucker,<sup>36</sup> D. Viganò,<sup>5,6</sup> N. Vittorio,<sup>21</sup>  
F. Wicek,<sup>4</sup> M. Wright<sup>28</sup> and A. Zullo<sup>2</sup>**

<sup>1</sup>Università di Roma — La Sapienza, Piazzale Aldo Moro, 5, 00185 Roma, Italy

<sup>2</sup>INFN sezione di Roma, Piazzale Aldo Moro, 5, 00185 Roma, Italy

<sup>3</sup>Astroparticule et Cosmologie, Université de Paris, CNRS,  
10 Rue Alice Domon et Léonie Duquet, 75013 Paris, France

<sup>4</sup>Laboratoire de Physique des 2 Infinis Irène Joliot-Curie CNRS-IN2P3,  
Université Paris-Saclay,  
Bât. 100, 15 rue Georges Clémenceau, 91405 Orsay cedex, France

<sup>5</sup>Università degli studi di Milano, Via Celoria 16, 20122 Milano, Italy

<sup>6</sup>INFN sezione di Milano, Via Celoria 16, 20122 Milano, Italy

<sup>7</sup>Department of Experimental Physics, National University of Ireland,  
Maynooth, Co. Kildare, Ireland

<sup>8</sup>Cardiff University, Cardiff CF10 3AT, U.K.

<sup>9</sup>INFN — Pisa Section, Largo Bruno Pontecorvo, 3/Edificio C, 56127 Pisa, Italy

<sup>10</sup>Observatoire de Paris, Université Paris Science et Lettres,  
61 Av. de l'Observatoire, F-75014 Paris, France

<sup>11</sup>Università di Milano — Bicocca, Piazza dell'Ateneo Nuovo, 1, 20126 Milano, Italy

<sup>12</sup>INFN Milano-Bicocca, Edificio U2, Piazza della Scienza, 3 — I-20126 Milano, Italy

<sup>13</sup>GEMA, Universidad Nacional de La Plata,  
Calle 116 y 48, La Plata, Argentina

<sup>14</sup>Instituto de Tecnologías en Detección y Astropartículas (CNEA, CONICET, UNSAM),  
Av. Gral Paz 1499 — San Martín, Argentina

<sup>15</sup>Centro Atómico Bariloche and Instituto Balseiro (CNEA),  
Av. Exequiel Bustillo 9500, San Carlos de Bariloche, Argentina

<sup>16</sup>Institut de Recherche en Astrophysique et Planétologie (CNRS-INSU),  
9 Av. du Colonel Roche, 31400 Toulouse, France

<sup>17</sup>Department of Physics, University of Oxford, Parks Rd, Oxford OX1 3PJ, U.K.

<sup>18</sup>Centre de Nanosciences et de Nanotechnologies,  
15 Rue Georges Clémenceau, 91405 Orsay Cedex, France

<sup>19</sup>Centro Atómico Constituyentes (CNEA),  
Av. Gral. Paz 1499, B1650 Villa Maipú, Argentina

<sup>20</sup>University of Richmond,  
Richmond, 410 Westhampton Way, Richmond, VA 23173, U.S.A.

<sup>21</sup>Dipartimento di fisica, Università di Roma — Tor Vergata,  
Viale della Ricerca Scientifica, 1, 00133 Roma, Italy

<sup>22</sup>INFN sezione di Roma2, Via della Ricerca Scientifica, 1, 00133 Roma, Italy

- <sup>23</sup>University of Surrey, Stag Hill, University Campus, Guildford GU2 7XH, U.K.
- <sup>24</sup>Facultad de Ciencias Astronómicas y Geofísicas, Universidad Nacional de La Plata, Paseo del Bosque S/N, B1900FWA La Plata, Argentina
- <sup>25</sup>Escuela de Ciencia y Tecnología (UNSAM) and Centro Atómico Constituyentes (CNEA), Tornavías Martín de Irigoyen No.3100, B1650 Villa Lynch, Argentina
- <sup>26</sup>IRFU, CEA, Université Paris-Saclay, Bât 141, F-91191 Gif-sur-Yvette, France
- <sup>27</sup>Institut d’Astrophysique Spatiale, Orsay (CNRS-INSU), Rue Jean-Dominique Cassini, 91440 Bures-sur-Yvette, France
- <sup>28</sup>University of Manchester, Oxford Rd, Manchester M13 9PL, U.K.
- <sup>29</sup>Italian Space Agency, Via del Politecnico snc 00133, Roma, Italy
- <sup>30</sup>Pontificia Universidad Católica de Chile, Av Libertador Bernardo O’Higgins 340, Santiago, Chile
- <sup>31</sup>Instituto Argentino de Radioastronomía (CONICET, CIC), Camino Gral. Belgrano Km 40, Berazategui, Argentina
- <sup>32</sup>Department of Physics, California Institute of Technology, Pasadena, CA 91125, U.S.A.
- <sup>33</sup>Consejo Nacional de Investigaciones Científicas y Técnicas (CONICET), Godoy Cruz 2290, 1425, Ciudad Autónoma de Buenos Aires, Argentina
- <sup>34</sup>Institute of Technology, Kilkenny Rd, Moanacurragh, Carlow, Ireland
- <sup>35</sup>Department of Physics, University of Wisconsin Madison, 1150 University Ave, Madison WI 53703, U.S.A.
- <sup>36</sup>Brown University, Providence, RI 02912, U.S.A.
- E-mail: [giuseppe.dalessandro@uniroma1.it](mailto:giuseppe.dalessandro@uniroma1.it), [lorenzo.mele@roma1.infn.it](mailto:lorenzo.mele@roma1.infn.it), [fabio.columbro@roma1.infn.it](mailto:fabio.columbro@roma1.infn.it)

Received November 25, 2020

Revised January 21, 2022

Accepted February 2, 2022

Published April 21, 2022

**Abstract.** Setting an upper limit or detection of B-mode polarization imprinted by gravitational waves from Inflation is one goal of modern large angular scale cosmic microwave background (CMB) experiments around the world. A great effort is being made in the deployment of many ground-based, balloon-borne and satellite experiments, using different methods to separate this faint polarized component from the incoming radiation. QUBIC exploits one of the most widely-used techniques to extract the input Stokes parameters, consisting in a rotating half-wave plate (HWP) and a linear polarizer to separate and modulate polarization components. QUBIC uses a step-by-step rotating HWP, with  $15^\circ$  steps, combined with a  $0.4^\circ\text{s}^{-1}$  azimuth sky scan speed. The rotation is driven by a stepper motor mounted on the cryostat outer shell to avoid heat load at internal cryogenic stages. The design of this optical element is an engineering challenge due to its large 370 mm diameter and the 8 K operation temperature that are unique features of the QUBIC experiment. We present the design for a modulator mechanism for up to 370 mm, and the first optical tests by using the prototype of QUBIC HWP (180 mm diameter). The tests and results presented in this work show that the QUBIC HWP rotator can achieve a precision of  $0.15^\circ$  in position by using the stepper motor and custom-made optical encoder. The rotation induces  $< 5.0\text{ mW}$  (95% C.L.) of power load on the 4 K stage, resulting in no thermal issues on this stage during measurements.

We measure a temperature settle-down characteristic time of 28 s after a rotation through a  $15^\circ$  step, compatible with the scanning strategy, and we estimate a maximum temperature gradient within the HWP of  $\leq 10$  mK. This was calculated by setting up finite element thermal simulations that include the temperature profiles measured during the rotator operations. We report polarization modulation measurements performed at 150 GHz, showing a polarization efficiency  $> 99\%$  (68% C.L.) and a median cross-polarization  $\chi_{\text{Pol}}$  of 0.12%, with 71% of detectors showing a  $\chi_{\text{Pol}} + 2\sigma$  upper limit  $< 1\%$ , measured using selected detectors that had the best signal-to-noise ratio.

**Keywords:** CMBR detectors, CMBR experiments, CMBR polarisation, gravitational waves and CMBR polarization

**ArXiv ePrint:** [2008.10667](https://arxiv.org/abs/2008.10667)

---

## Contents

<b>1</b>	<b>Introduction</b>	<b>1</b>
<b>2</b>	<b>Comparison with other experiments</b>	<b>2</b>
2.1	Similarities and novelty	3
<b>3</b>	<b>Strategy and requirements</b>	<b>4</b>
<b>4</b>	<b>Mechanical implementation</b>	<b>5</b>
4.1	Motor and transmission	5
4.2	Pulley system	6
4.3	HWP support	7
4.3.1	HWP thermalization	7
<b>5</b>	<b>Position read-out</b>	<b>8</b>
5.1	Electronics	8
5.2	Control software	9
<b>6</b>	<b>Mechanical test</b>	<b>10</b>
6.1	Liquid nitrogen	10
6.2	QUBIC cryostat	10
<b>7</b>	<b>Thermal performance</b>	<b>12</b>
7.1	Characteristic time constant and heating during operation	12
7.1.1	HWP temperature	15
<b>8</b>	<b>Optical properties</b>	<b>15</b>
8.1	A model for the QUBIC-TD polarimeter	16
<b>9</b>	<b>Polarization modulation</b>	<b>17</b>
9.1	$\chi$ -polarization	19
9.2	Results	21
<b>10</b>	<b>Conclusions</b>	<b>22</b>

---

## 1 Introduction

The Q&U Bolometric Interferometer for Cosmology (QUBIC) is a ground-based experiment which aims to measure the polarization of the cosmic microwave background (CMB). QUBIC uses bolometric interferometry, a novel concept that combines the calibration control and beam synthesis capabilities of interferometers with bolometric detectors. The main goal of the QUBIC instrument is to improve current constraints on a characteristic polarization pattern hidden in the CMB, known as the primordial B-mode polarization [1]. This component is believed to have been imprinted via non isotropic Thompson scattering induced in the primordial plasma perturbed by inflationary gravitational waves. The tensor-to-scalar ratio  $r$ , which measures the relationship between the amplitudes of the power spectrum of tensor and scalar fluctuations, is generally used as the observable and to date only an upper limit of  $r < 0.036$  at 95% confidence has been set in Ade et al. [2]. Stronger upper limits, or robust detection, must contend with instrumental systematic effects as well as foreground sources of

emission within our Galaxy. QUBIC is capable of controlling some systematic effects via its so-called *self-calibration* procedure [3, 4]. As with every ground-based experiment, due to the Earth’s atmosphere, QUBIC can only perform sky observations in a few frequency bands, but it can mitigate this problem by separating the CMB signal from polarized foregrounds via its spectral-imaging capabilities [5] and [6]. This unique feature of the QUBIC instrument allows the signal to be extracted in frequency sub-bands within the main bands, with a spectral resolution of  $\Delta\nu/\nu \sim 0.05$  [5], helping us to characterize and remove galactic foregrounds. The optical design of QUBIC, described in details in O’Sullivan et al. [7], is optimized around its key component, the beam combiner. This is the core of the bolometric interferometer and it is realized using 400 back-to-back corrugated feedhorns, each pair being coupled with a controllable blocking blade [8]. The interference pattern produced by the horn array leads to synthesized images on two orthogonal focal planes tiled with arrays of bolometric detectors. The capability of excluding single back-to-back horn pairs allows the self-calibration procedure to be performed [9]. Each array has 1024 transition edge sensors (TES) with a noise equivalent power (NEP) of  $10^{-16}\text{W}/\sqrt{\text{Hz}}$  described in Piat et al. [10], limited by the cooler microphonics. Two frequency bands are selected using a dichroic filter, which reflects radiation at 220 GHz and transmits radiation at 150 GHz onto the two focal planes.

Many techniques have been developed to measure the weak polarized signal coming from the cosmological microwave radiation, for example the BICEP experiment [11] uses pair-differencing of polarization sensitive detectors together with boresight rotation of the whole experiment. New strategies have been developed, such as for the PIXIE experiment [12] which simultaneously measures the polarization and spectrum of the CMB. In QUBIC, polarization measurement is done using a polarimeter [13], as it is in MAXIPOL [14].

The QUBIC polarimeter is composed of a retarder plate, a half-wave plate (HWP), which induces a phase shift between the two orthogonal polarization components, coupled with a linear polarizer that is used as polarization selector. By rotating the HWP, it is possible to modulate the Stokes vector components. This polarization modulation methodology is used by a large number of CMB experiments: MAXIPOL [14], EBEX [15], SPIDER [16], LSPE [17] and [18] and ACT-Pol [19], among others.

In this paper, we report on the design and the performance of the cryogenic polarimeter developed for the QUBIC experiment. In section 2 we make a comparison with other experiments to point out the novelty of the system. Section 3 shows the scanning strategy and instrumental constraints, while section 4 describes the mechanism that allows for rotation at cryogenic temperatures. Section 5 shows the custom-built absolute encoder used to recover the HWP orientation. In section 6 we report on all the mechanical tests that were performed in order to improve the mechanics of the device before its implementation in the QUBIC cryostat. The first tests in the cryostat are also described in this section. Sections 7 to 9 describe the optical and thermal performances of the system. The current version of the experiment is a Technological Demonstrator Instrument (TD), described in Torchinsky et al. [20], composed of a reduced array of 64 back-to-back feed-horns, one-quarter of the 150 GHz detector array, and HWP with a reduced diameter with respect to the one which will be used in the Full Instrument (FI).

## 2 Comparison with other experiments

The use of a Stokes polarimeter composed by a retarder plus a polarizer is a standard strategy for polarization measurement. The equation for the signal from a polarimeter that uses a

Experiment	frequency	clear aperture $\varnothing$ [mm]	HWP temp.
<b>QUBIC</b>	1/85 s	370	<10 K
SPIDER [25]	1/day	305	<10 K
EBEX [21]	<2 Hz	100	<10 K
PILOT [26]	1/11.4 s	50	<10 K
BLAST-POL [27]	>1/6 s	105	120 K
POLARBEAR [28, 29]	>2 Hz	440	50 K
ACT-POL (ABS) [22]	2.5 Hz	324	Room temp.
NIKA [23, 30]	3 Hz	100	Room temp.
NIKA2 [24, 30]	$\sim$ 3 Hz	200	Room temp.

**Table 1.** Experiments equipped with a HWP to modulate the input polarization, ordered by operating temperature.

rotating HWP allows us to separate the first three components of the Stokes vector T, Q, and U:

$$I = \frac{1}{2} [T + Q \cos(4\theta) + U \sin(4\theta)]. \quad (2.1)$$

The HWP can rotate continuously or step-by-step, depending on the experiment scanning strategy. MAXIPOL [14] and, a few years later, EBEX [21] were the first experiments to use a continuously rotating HWP located in the optical systems aperture stop. The aperture stop, however, was not the first element along the optical path. ABS [22], NIKA [23] and NIKA2 [24] placed a continuously rotating HWP between the sky and the instrument in order to modulate only the sky polarization. SPIDER [25] and QUBIC place the HWP skyward, to not modulate instrumental spurious polarization, and at a cryogenic temperature, to reduce the polarized emission of the HWP. Both SPIDER and QUBIC modulate the sky by moving the instrument, in addition to the HWP modulation. The QUBIC final instrument mount also allows a boresight rotation of  $\pm 15^\circ$ , and so combines the advantages of using HWP and boresight rotation. In table 1 many experiments which used/use<sup>1</sup> a HWP are listed. The table shows that when fully implemented QUBIC-FI will have the largest clear aperture for its strategy and temperature of operation. In QUBIC-TD the clear aperture is only 180 mm, but it is implemented with a 370 mm rotational mechanism.

## 2.1 Similarities and novelty

During the design phase, it was decided to use a mix of established technologies for the HWP mechanics, such as those adopted by the PILOT [26] and the EBEX [31] experiments. This design was selected as a faster and more reliable design option, without the amount of R&D needed for a cryogenic continuously rotating HWP.

There are a few similarities between the QUBIC, EBEX and PILOT polarization modulation units. All use a fiberglass shaft to transmit the torque from the outer shell of the cryostat to the cryogenic stage below 10 K. While PILOT rotates a small diameter HWP with an endless screw, QUBIC and EBEX have a stainless steel and a kevlar belt, respectively. As for the bearing, EBEX has a superconducting levitating rotor and the belt is used only

<sup>1</sup>Only experiments deployed already are shown in the table 1.

to transmit the torque at the beginning after which the rotor is free to spin with very low friction. In QUBIC, the belt actuates the rotation of each step.

Both QUBIC and EBEX has passive control of differential thermal contractions, see sections 4.2 and 4.3, which are not used in PILOT. QUBIC differs from SPIDER in the position of the stepper motor: in SPIDER the motor is placed at the cryogenic stage, having the advantage of using a short shaft to transmit the torque and the disadvantage of increasing the power load on the cryogenic stage due to the motor rotation. SPIDER, like PILOT, uses an endless screw to rotate the HWP while QUBIC uses a pulley plus belt system allowing to rotate the HWP.

### 3 Strategy and requirements

QUBIC will observe a sky patch at mid galactic latitudes in the southern hemisphere, that has an extent of  $35^\circ$  in azimuth and  $40^\circ$  in elevation, and that includes the BICEP2 region (RA =  $0^\circ$ , dec =  $-57^\circ$ ) and the Planck clean field (RA =  $8.7^\circ$ , dec =  $-41.7^\circ$ ). QUBIC will scan the sky by moving in azimuth at a speed of  $0.4^\circ/\text{s}$  and will change the HWP position after each scan. In addition to the time required to perform a complete azimuthal scan (85 s),  $\sim 5$  s more are required to decelerate the mount and change direction, adding  $2.5^\circ$  to the azimuth scan. Since the slewing time is spent out of the main sky-patch, the observed sky is composed of the main patch plus a slewing patch. QUBIC will use the slewing time to step the HWP angle by  $15^\circ$ . The HWP angular precision requirement has been determined by dedicated simulations which confirm results showed in Buzzelli et al. [32], Aumont et al. [33] and Pagano et al. [34], setting the requirement to  $<0.2^\circ$  due to E $\rightarrow$ B level of contamination that must match the QUBIC intended limits on r. Once the azimuth scans have been performed at each HWP nominal position ( $0^\circ$ ,  $15^\circ$ ,  $30^\circ$ ,  $45^\circ$ ,  $60^\circ$ ,  $75^\circ$ ,  $90^\circ$ ), the elevation of the alt-azimuth mount is changed. While the main patch is observed with a nominal orientation of the HWP, the slewing patch is observed while the HWP is moving, performing a  $15^\circ$  step. QUBIC will also spend part of its observing time performing self-calibration as in Bigot-Sazy et al. [9]. This procedure, combined with the possibility of rotating the instrument around its optical axis (boresight axis), helps monitor systematic effects. Its systematic error control and TES sensitivity [10] will allow the QUBIC FI to put an upper limit on the tensor-to-scalar ratio of  $r < 0.013$  [1] at 95% CL assuming two years of integration, a 30% efficiency that is related to the observational site, and a 50% duty cycle between observations and self-calibration.

Rotating a large optical element at cryogenic temperatures is not easy because of the increased friction between two co-moving parts. Moreover, different materials, typically used in rotating bearings for instance, contract differently during the cool-down. A problem related to the rotation is the thermal load dissipated by the rotation itself. A temperature gradient across the HWP arises due to a combination of the frictional power load dissipated during the rotation and the thermal conductivity between the HWP and its cryogenic stage (4 K for QUBIC [35]). This gradient, before and after the rotation, should be stable to a mK level. Another issue caused by the friction is the heating of the cryogenic stage where the HWP is placed: the cool-down time of the stage has to be lower than the HWP stepping period.

A possible solution to minimize these effects is to implement a levitating HWP (adopted by experiments such as EBEX [21, 31] and LiteBIRD [36, 37]). In this configuration the HWP is held by a permanent magnet ring which levitates above a superconductor and can therefore spin continuously with very low friction.

The QUBIC HWP rotator has been designed to satisfy these requirements:

- speed  $> 3^\circ/\text{s}$ ; from slewing  $15^\circ$  in the 5 sec turnaround time for the azimuth scans
- orientation accuracy  $< 0.2^\circ$ ; from E- $\rightarrow$ B contamination,
- thermal load lower than 10 mW at the operating temperature; from experiment thermal budget, see section 2.3.2 in Masi et al. [35]
- 4 K stage settle-down time, after one HWP rotation, of  $< 85$  s.

## 4 Mechanical implementation

The QUBIC cryostat, described in Masi et al. [35], figure 1, is composed of three temperature stages: the vacuum shell at room temperature, the 40 K shield, and the 4 K shield. The internal shields are cooled by means of two parallel pulse tube cryocoolers. The vacuum shell is 1.5 m tall and 1.4 m diameter aluminum cylinder with an ultra-high molecular weight (UHMW) [38] polyethylene window followed by two infrared (IR) filters. There are three IR filters along the light path at the 40 K shield, which is separated from the vacuum shell by 30 super insulation layers. There is one reflecting metal mesh filter and one absorptive low pass filter with a  $12 \text{ cm}^{-1}$  roll off frequency at the 4 K shield. Below this last filter, there is the HWP and the polarizer. The temperature reached by the upper part of the 4 K shield is always between 8 and 10 K. Inside the 4 K shield there are two adsorption refrigerators: a  $\text{He}^4$  adsorption refrigerator, which cools down the optics box and the back to back horn array to 1 K, and a  $\text{He}^7$  adsorption refrigerator, which cools down the detectors to  $\sim 340$  mK.

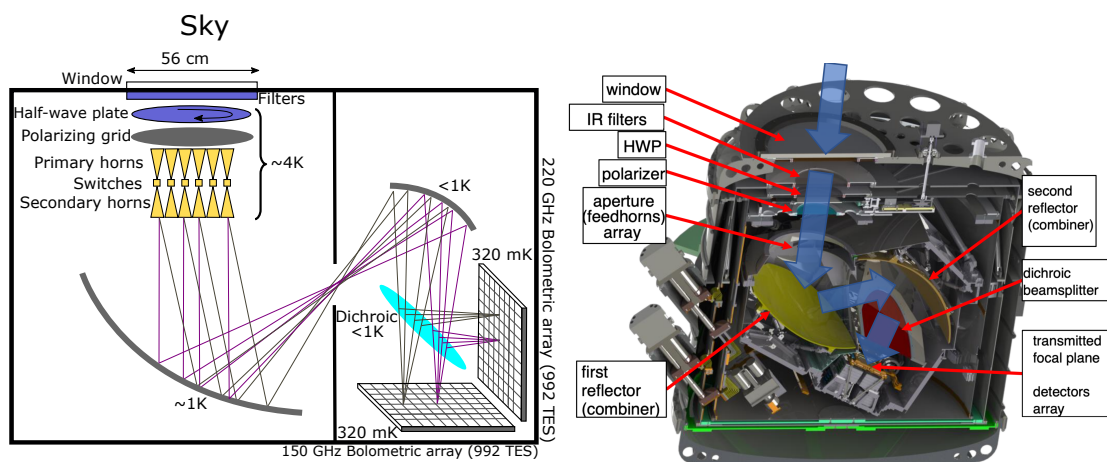
The two mirrors make the system a Fizeau interferometer coupled with the sky with the back-to-back horn array. Each horn aperture is the aperture stop of the experiment and they are placed 82.3 mm from the HWP and at 324 mm from the window.

Figure 2 shows a 3D CAD model of the cryogenic HWP rotator. It is placed at the top of the 4 K stage, after the IR blocker filters, as described in Masi et al. [35]. The most important components are the transmission system, the pulley system and the HWP support. The rotation is produced by an external stepper motor, placed on the top of the cryostat vacuum shell. It is transmitted to the HWP, on the top of the 4 K stage, through two magnetic joints and a fiberglass tube shaft combined with a system of pulleys and a stainless steel belt. All the parts composing the rotator are described in details in the following subsections.

### 4.1 Motor and transmission

In order to reduce the thermal load at the cryogenic stage where the HWP is placed, the motor is placed outside the vacuum vessel at room temperature. The stepper motor is a Sonceboz 6600-30 Hybrid stepper motor,  $1.8^\circ$  per step and  $\sim 2 \text{ N m}$  torque. The transmission ratio between the motor and the HWP support is determined by the pulleys and allows us to move the HWP by  $0.003^\circ$  per motor step. Since the motor is placed outside the vacuum vessel, we use two magnetic joints to transfer the rotation from the motor to the solid cylindrical shaft, which is made of G-10 and is 10 mm diameter, 140 mm in length and 1 mm thick. This transmits the rotation from the motor, at room temperature, to the transmission belt, at the 4 K stage. The measured thermal load due to the shaft is a few mW.

The transmission belt is a stainless steel braid,  $\sim 1.4$  m long and 0.6 mm wide. It surrounds the HWP support ring and the pulley system. In a previous version of the design a



**Figure 1.** Schematic of the QUBIC instrument (left) and sectional cut of the cryostat (right) showing the same sub-systems in their real configuration.

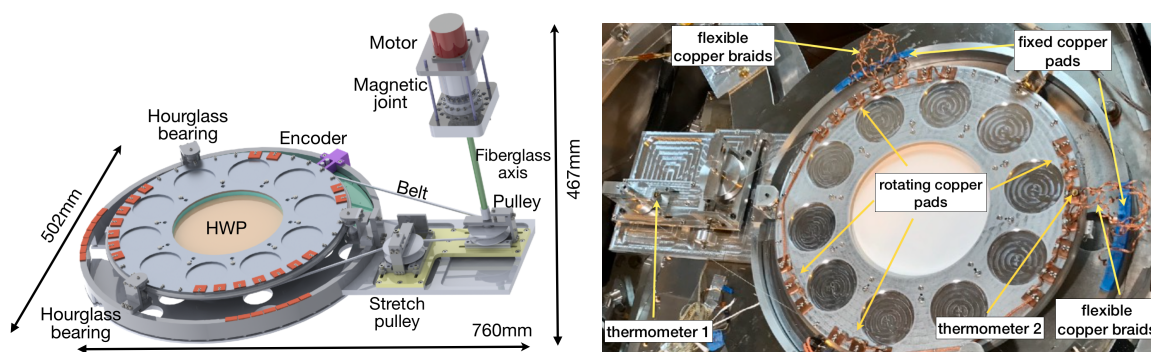


**Figure 2.** Left: rendering of the HWP rotator mechanism. Right: thermalization system: the fixed copper pads are connected to the rotating ones with flexible copper braids.

kevlar belt was used, but after several tests in liquid nitrogen the kevlar belt was replaced by a stainless steel one due to its lower differential thermal contraction with respect to aluminum which is the main material used for the rotation mechanism.

## 4.2 Pulley system

The pulley system is composed of two aluminum pulleys which help the belt transmit the rotation from the motor to the HWP support. The first pulley, figure 3, is directly connected to the fiberglass shaft. In the first test at liquid nitrogen temperature we noticed that the friction between the belt and this pulley was so small that during the rotation the belt slipped in its groove in the pulley. To improve the friction, the pulley was shaped with a helicoid groove in order to make the belt perform at least three revolutions around the pulley. The second pulley, also called the stretch-pulley, is mounted on a spring-loaded sliding support that acts as a tensioner. The pulley is in equilibrium between the belt and the spring tensions. From the differential thermal contraction point-of-view, the belt contracts more than the other parts. The stretch-pulley aims to recover all the differential contractions between the belt and the other parts. We tuned the spring tension during the test in liquid nitrogen (77 K) and details of this procedure are reported in section 6.1.

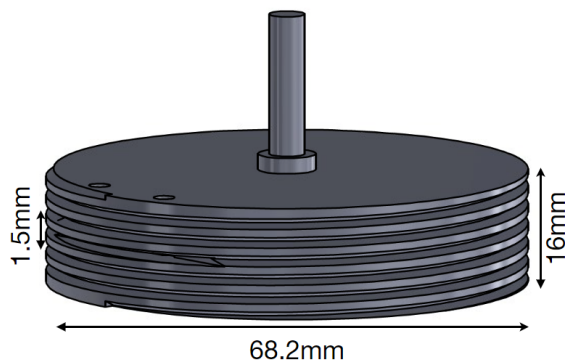


**Figure 3.** The first pulley has been shaped with a helicoid groove, 1.5 mm step, to make the belt perform at least three revolutions around the pulley.

In section 6 we show how the proper operation of the stretch-pulley was verified while it was operating inside the cryostat. Similar care is taken in EBEX [21], where a kevlar belt, instead of stainless steel one, is used to transmit the rotation while the HWP is suspended on magnetic bearings, instead of classic thrust bearings.

### 4.3 HWP support

The HWP support is a ring-shaped aluminum flange suspended by three hourglass-shaped bearings made of stainless steel, shown in figure 4 (right). The HWP diameter for the TD is 180 mm, while for the FI it will be  $\sim 370$  mm. The aluminum flange profile has been manufactured with a half-circle shape to produce less friction with the bearings. The hourglasses are squeezed by a couple of thrust bearings fixed with Belleville spring washers to leave them free to contract and to prevent them from getting stuck, as shown in the right panel of figure 4. We regulate the spring washer tension at 77 K in order to have smooth rotation and reduce friction inside the bearings.

An important part of the HWP support is the clamping system, shown in figure 4 (left): it is not possible to clamp the HWP directly on the aluminum ring flange because they are made of different materials. The HWP is a 4.1 mm polypropylene disk that has an expansion coefficient greater than the aluminum. In order to prevent internal stresses and changes in its geometry at cryogenic temperature, the HWP was mounted inside a PEEK<sup>2</sup> ring. At 10 K the relative thermal contractions of polypropylene [39] and [40], PEEK [40] and aluminum<sup>3</sup> are 1.1%, 1.2% and 0.4% respectively. The PEEK ring is fixed to the aluminum ring with four stainless steel spheres. The spheres allow a floating contact only in the direction corresponding to the polarizer transmission axis, preventing variations in the orientation angle while the device is rotating.

#### 4.3.1 HWP thermalization

The thermalization of the HWP and its support is not possible using rigid conductors because it rotates with respect to other mechanical parts. We used 14 flexible copper braids between the HWP support and the nearest fixed ring. They guarantee a total thermal conductivity of  $46 \text{ mW K}^{-1}$  at 8 K. Other copper braids surround the HWP support to guarantee homogeneity.

<sup>2</sup>[https://www.victrex.com/-/media/downloads/datasheets/victrex\\_tds\\_450fe20.pdf](https://www.victrex.com/-/media/downloads/datasheets/victrex_tds_450fe20.pdf).

<sup>3</sup>[https://trc.nist.gov/cryogenics/materials/6061%20Aluminum/6061\\_T6Aluminum\\_rev.htm](https://trc.nist.gov/cryogenics/materials/6061%20Aluminum/6061_T6Aluminum_rev.htm).

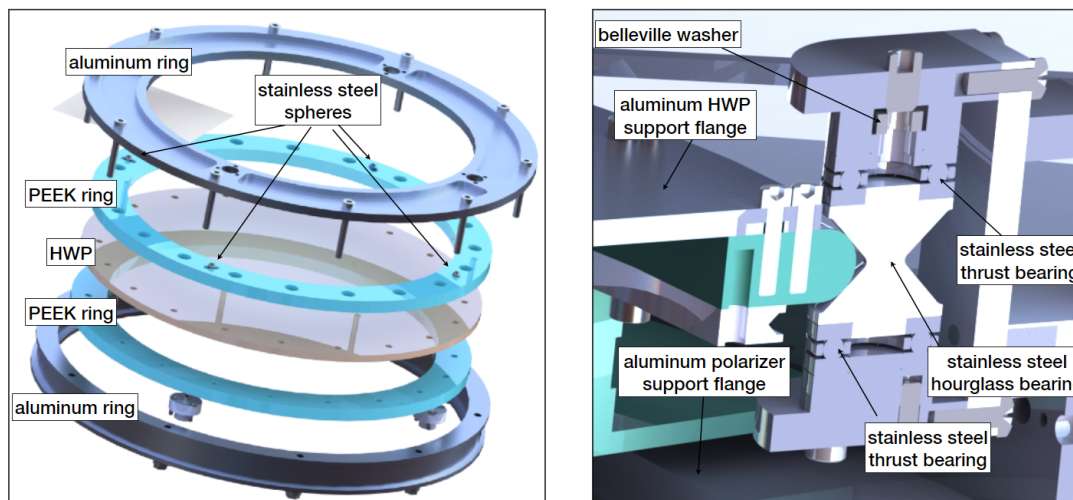


**Figure 4.** Left: the HWP clamping system is composed of a PEEK ring, shown in blue, floating on an aluminum ring using 4 spheres. Right: an hourglass bearing section help to minimize friction with the HWP support. The thrust bearings are squeezed with belleville washers to leave them free to contract. The HWP support is suspended by three such hourglasses equally spaced by  $120^\circ$ .

All the copper braids end with an oxygen-free high-conductivity (OFHC) copper pad fixed with silver glue.

The thermalization system is shown in figure 2. During cool-down in nitrogen, see section 6, we measured a temperature gradient of less than 0.1 K between the stator and the rotor. We repeated the measurement for several positions with the same results.

## 5 Position read-out

The optical encoder, already used in PILOT [26], allows the  $90^\circ$  of rotation to be separated into seven positions, equally spaced by  $15^\circ$ . The readout system is composed of a custom optical encoder, where three pairs of optical fibers face each other, and each pair transmits modulated IR light. The absolute encoder is made of a precisely manufactured metal plate where binary-coded pattern of holes, 2 mm in diameter, define seven positions. The holes were machined with  $<5\ \mu\text{m}$  precision in positioning, diameter, and hole pattern alignment. The alignment of the plate with the optical fiber support determines the orientation accuracy of the rotation system.

### 5.1 Electronics

The electronics are used to recover the rotator position by reading the signals from the optical fibers of the absolute encoder. The signal is first generated by an oscillator, mounted on a printed circuit board (PCB), and it is then converted into IR signals by three transmitters which are directly connected to the three primary optical fibers. The signal passes from the three primary fibers to the three secondary ones once the fibers and the holes patterns on the gearwheel are aligned. The signal from the secondary fibers is detected by three photodiodes and amplified using lock-in amplifiers. The combination of the signals from these lock-in

amplifiers is used to recover the HWP orientation according to eq. (5.1):

$$Pos = \sum_{N=0}^{N=2} Bit_N \cdot 2^N \quad Bit_N = 0, 1 \quad (5.1)$$

where the variable  $Bit_N$  is equal to zero or one, depending on whether the light is interrupted or transmitted, respectively.

The transmitters<sup>4</sup> wavelength of operation is tuned to 820 nm by maximising the signal amplitude. The signal transmitted to the fibers is modulated at 1 kHz by the oscillator and is in the end extracted from uncorrelated noise by a custom synchronous demodulator based on AD630 lock-in amplifiers. The use of lock-in demodulation is necessary because of the significant light loss from the gap of about 7 mm between the primary and the secondary fibers and the resulting reduction in the signal to noise ratio. The signals from the lock-in amplifiers are processed by a custom firmware running on a Raspberry Pi3<sup>5</sup> (RbPi), which recovers the HWP position by continuously reading the lock-in signals. The RbPi also controls the stepper motor, rotating the HWP in accordance with the scan strategy on the sky. The transmitters and the photodiodes are housed in an electronics box on a bracket inside the 300 K vacuum shield while the PCB, the motor drive system and the RbPi are placed in an external electronic box.

## 5.2 Control software

The firmware was developed in Python<sup>6</sup> and runs continuously on the RbPi. A user datagram protocol (UDP) is used to communicate between QUBIC-studio [20] and the RbPi. QUBIC-studio is an interface system used to control each individual subsystem of the experiment. A connection is established when the RbPi is turned on and it is controlled by a watchdog every minute. When the connection is established, the RbPi remains on hold until it receives a command from QUBIC-studio. The core of the firmware consists of three main functions which allows us to calibrate the rotator in terms of the number of motor steps needed to reach each position and to move the rotator according to the scanning strategy:

- HOME: Find the 1<sup>st</sup> position at  $\theta = 0^\circ$  from any starting position
- CAL #: Performs # scans counting the number of motor steps to reach the nominal positions
- GOTO #: Moves the rotator to the position number # (# ranges between 1 and 7)

The HOME function is necessary since the HWP rotator is located on the top of the 4 K stage and it is not visible. The only way to test the rotator operation is through the position readout system which provides the HWP orientation when the optical fibers and the hole patterns on the gearwheel align. The CAL function calibrates the number of motor steps that the rotator needs to take to reach the nominal positions. Given the reproducibility of the motor steps measured during calibrations at 8 K, as it is reported in section 6.2. Counting of the motor steps allows the HWP to be moved to intermediate positions, allowing us to acquire data between HWP nominal positions, providing a better estimate of the Stokes parameters from the measured polarization modulation curve.

<sup>4</sup>AVAGO Technologies model HFBR-1412TMZ.

<sup>5</sup><https://www.raspberrypi.org>.

<sup>6</sup><https://www.python.org>.

After calibration of the number of motor steps, the HWP position can be changed with a series of GOTO commands. The integration time on each single position is determined by the scanning strategy. Minor functions are called within the three main functions to set basic rotation parameters, such as its direction and velocity, which are optimized for the scanning strategy.

## 6 Mechanical test

The HWP rotator has been tested under several conditions: at room temperature on an optical bench mainly for the firmware debugging [6], in liquid nitrogen in order to fine tune the stretch-pulley tension at a temperature close to its final working temperature, and, finally, in its cryostat at a temperature of 8 K.

During room temperature calibrations, we measured the HWP tilt angle with respect to the optical axis with a Mitutoyo micrometer position sensor. The measurements are repeated at different HWP nominal positions. The planarity of the HWP support was measured as well, to disentangle the contribution to the HWP tilt produced by a non-flat HWP support. These two measurements permitted to retrieve a total wobbling angle less than  $0.1^\circ$ , limiting the related systematic effect as described in D’Alessandro et al. [41]. Details of the rotator performance during the last two test phases are reported in the sections below.

### 6.1 Liquid nitrogen

In order to verify the correct functionality at low temperatures, the rotator was cooled to liquid nitrogen temperature (77 K). The tests were performed in a big insulated tank, made of aluminum walls with an insulating foam core, filled with liquid nitrogen. The upper part of the tank was made of plexiglass allowing visual inspection and hand-tensioning of the stretch-pulley at a temperature of 77 K. This calibration should guarantee proper functioning at  $\sim 8$  K since the thermal contraction of the aluminum parts stabilizes below  $\sim 100$  K [42]. These tests were useful to understand the behaviour of the rotator in a cryogenic environment and allowed its performance to be improved by upgrading two mechanical aspects:

- the kevlar transmission belt has been replaced with one made of stainless steel,
- the shape of the first pulley has been changed in order to improve the friction between the pulley and the belt.

By using different magnetic joints we measured a torque of  $\sim 0.1$  N m to rotate the device at 77 K. In a worst case scenario where all the power needed to perform the rotation is dissipated by friction, the thermal load due to the rotation is 2.6 mW moving the HWP at  $7.5^\circ/\text{s}$ .

### 6.2 QUBIC cryostat

After the preliminary tests and mechanical improvements described so far, the rotator was installed in its nominal location inside the QUBIC cryostat. Two thermometers were placed on the HWP support ring and near the HWP for temperature monitoring. During the tests, the thermometers measured an equilibrium temperature of about 8 K, as reported in figure 7. The tests were performed by moving the HWP to the 7 nominal positions in steps of  $15^\circ$ , with the rotator velocity set to  $7.5^\circ/\text{s}$ .

The number of motor steps and the rotator position were acquired automatically by the RbPi and are reported in figure 5 (top), where 10 clockwise rotations performed at cryogenic

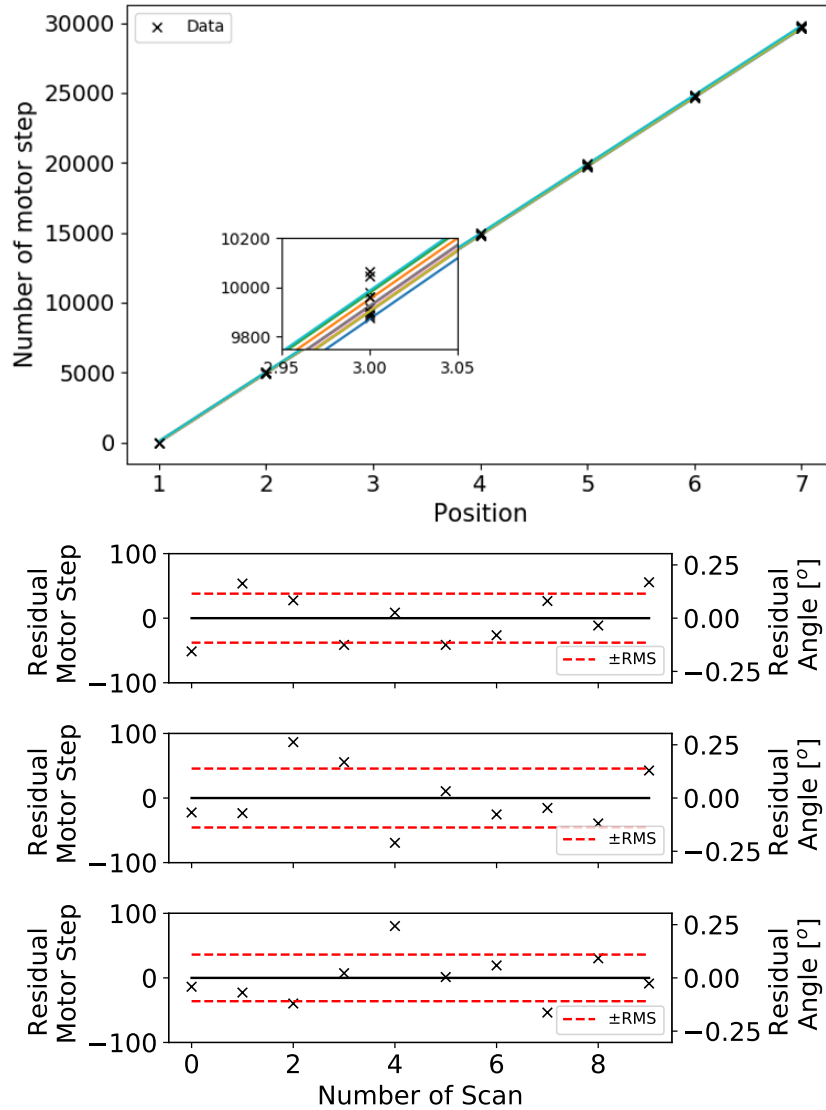


**Figure 5.** Top panel: number of motor steps with respect to the rotator positions, with corresponding linear fits acquired during 10 clockwise calibrations performed at 8 K inside the QUBIC cryostat. Bottom panel: residuals between the data and their average at each HWP position, reported in terms of motor steps and rotation angles for the 2nd, 3rd and 4th nominal positions as representative cases (from top to bottom sub-panels) from 10 clockwise calibrations.

temperatures are shown, together with the corresponding linear fits. In the same figure we show a close-up of the data around the 3rd position to better highlight the reproducibility in positioning. The bottom panel of figure 5 shows the residuals between the motor steps needed to reach positions 2, 3 and 4 (from top to bottom sub-panels) and their mean value. The absolute value of the measured fluctuations are always  $< 100$  motor steps ( $< 0.3^\circ$ ) with a root mean square (rms) value  $< 50$  motor steps ( $< 0.15^\circ$ ). About 100 motor steps ( $0.3^\circ$ ) of backlash were detected during the first cryogenic calibration measurements at the end positions 1 and 7, when the rotation is reversed. This effect is produced by the steel belt that was not tightened sufficiently. The effect is negligible if the rotator is moved to the nominal positions only, since in this case the positioning is independently provided by the readout

system, with a precision on the HWP orientation driven by the 3-bit hole alignment with the series of optical fibers. We neglect this effect as the data showed here were acquired at nominal positions only.

The size of each of the 7 nominal positions is measured by counting the number of motor steps taken during the time that the optical fiber signal can travel through the 3-bit holes, before further rotation takes them out of alignment. The average value of the size of the nominal positions has been measured to be  $0.2^\circ - 0.3^\circ$ , depending on the hole combination defining the position. To be conservative, we can assume that the error made on the orientation at the nominal positions is approximately half of the position size,  $\leq 0.15^\circ$ . This systematic error in positioning is comparable to the root mean square of the motor step fluctuations in the bottom panel of figure 5, extrapolated over several rotations. The backlash, if not quantified, is a potential source of error when the rotator is moved to any position which lies between the nominal ones, since they cannot be independently provided by the readout system and can only be extrapolated by counting motor steps. Position data taken in this configuration are affected by a global shift that can be quantified from the rotator calibration data, since the rotator works in a linear regime once the backlash is recovered. By fitting the rotator calibration data, and discarding the first few degrees of rotation affected by the backlash, a correction can be applied to the data thereby minimizing the source of error.

The measurements reported are representative cases, the same performance is achieved for the counterclockwise rotation and at all the nominal positions.

## 7 Thermal performance

The HWP rotation is transmitted to the HWP support ring with the friction generated in the transmission chain. Power is lost due to friction in the transmission of motion between the motor and the HWP; this power is dissipated in the form of heat, producing heating of the cryogenic stage.

In figure 6 we show the 4K filter temperature behaviour while the HWP is moving position by position. During regular scans, the motion of the mechanism produces typical 4K filter temperature fluctuations of  $<5$  mK *rms* that is correlated with the motion, while all the other thermometers are insensitive to this motion.

HWP heating impacts the detector sensitivity: the higher the temperature, the larger the power emitted and therefore the larger the thermal background on the focal plane. Due to the high emissivity of the HWP ( $\sim 3\%$ ) relative to filters and other optical elements ( $\ll 1\%$ ) it is important to keep its temperature low [43]. In this section the thermal effect of the rotation is analyzed by means of data acquired by a thermometer mounted near the HWP (Thermometer 2 in figure 2). Since a direct measurement of the HWP temperature is not easy to achieve, i.e. de Bernardis et al. [44], we use a finite element analysis to calculate a maximum temperature gradient inside the HWP.

### 7.1 Characteristic time constant and heating during operation

Due to the heat produced by friction during its rotation, the rotor heats up from its equilibrium temperature, producing a temperature that varies as a function of time  $T(t)$ . In order to understand the temperature behaviour of the rotating components, the rotator position was changed sequentially, from the 1st to the 7th, and then directly back to position 1. Each rotation is performed every  $\sim 15$  min while the whole test lasts more than half a day. A thermometer (Lakeshore DT-670, thermometer 2 in figure 2) was connected to the aluminium

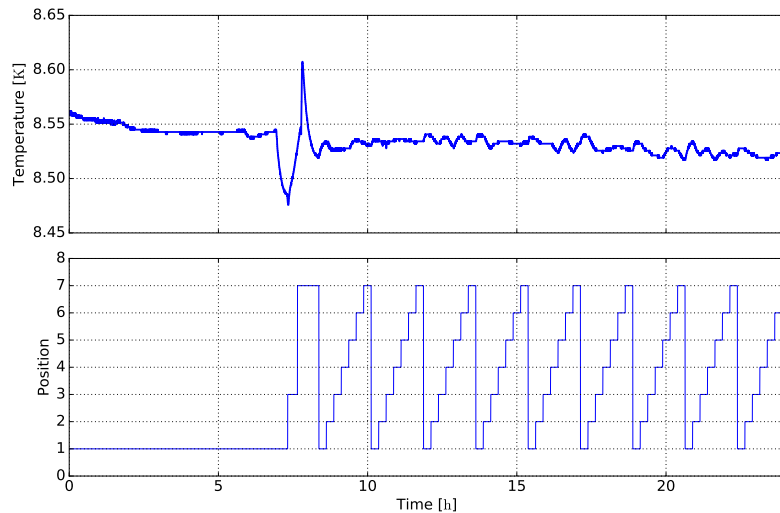


**Figure 6.** Temperature measured by the thermometer mounted on the 4 K filter, which is closest to the HWP rotation mechanism, compared with the HWP position during the movement of the mechanism (Masi et al. [35]).

bearing of the HWP. During these scans the thermometer mounted on the 4 K filter stage close to the rotator does not measure any significant variation. The temperature  $T_B \sim 8$  K of the stage is therefore assumed to be a constant. The top panel of figure 7 shows the thermometer 2 temperature detected close to the HWP (continuous black line) taken during two sample scans while the bottom panel shows the position data read by the absolute encoder. The change of the HWP position is related to a jump in the temperature profile, which quickly reaches a temperature  $T^*$  and, after the position is reached, starts to drop down again with an exponential decay. We analyzed the long term variation of the rotator temperature using a linear fit performed over a long acquisition time ( $\sim 15$  h). This linear fit (black dashed line in the top panel of figure 7) has a slope of  $-1.03 \text{ mK h}^{-1} \pm 0.03 \text{ mK h}^{-1}$  which means that the rotator is not heating up during the scans but is still being slowly cooled down by the pulse tubes.

The thermal model which describes the cool-down of the rotator after the heating induced by the motion follows the thermodynamic equation:

$$C \frac{d[T(t) - T_B]}{dt} = -K[T(t) - T_B] \quad (7.1)$$

where  $C$  is the heat capacity of the rotator and  $K$  is the thermal conductivity multiplied by the separation distance between the rotator and the 4 K stage. Data were interpolated using the following exponential solution:

$$T(t) - T_B = C^* e^{-\frac{Kt}{C}} \quad (7.2)$$

where  $C^*$  is related to the temperature rise induced by the rotation and  $\tau = \frac{C}{K}$  is the characteristic time constant.

Since the scanning strategy for QUBIC involves moving the HWP from one position to the next (i.e. position-by-position from 1 to 7, and then back again to position 1 in the same sense), the small temperature jumps are the most representative for the thermal behaviour of

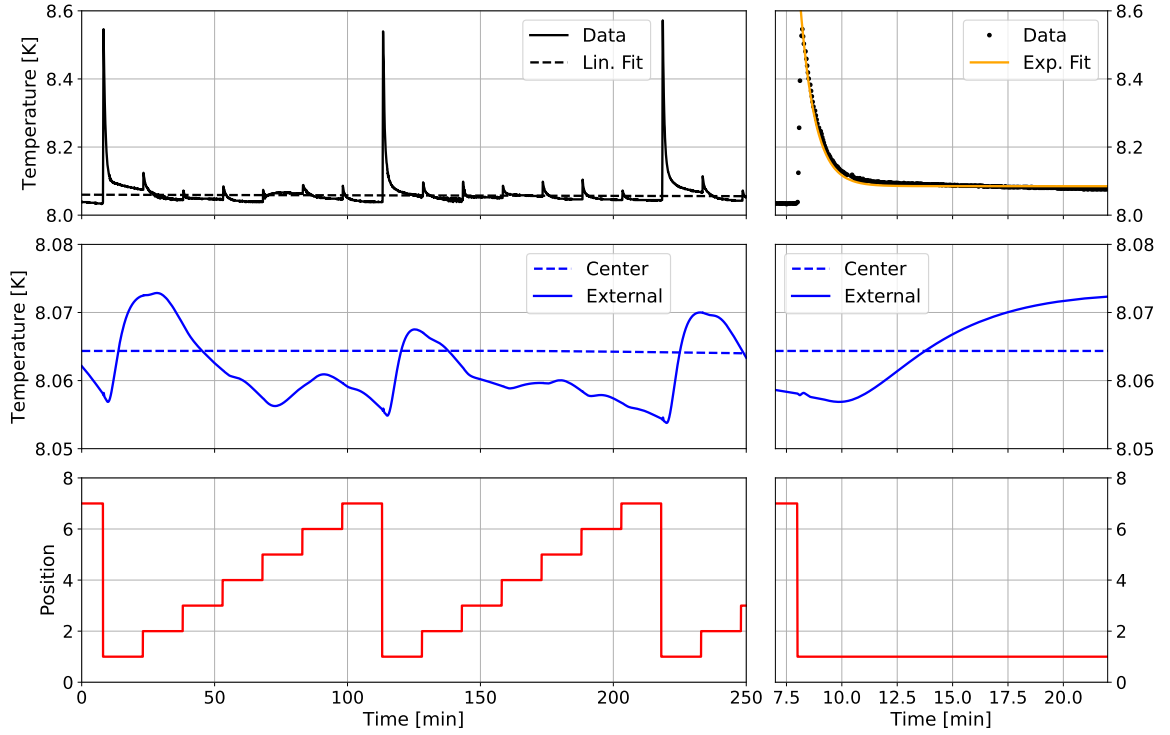


**Figure 7.** Top panels: temperature of the HWP aluminum bearing (black continuous line) and the linear fit (black dashed line) to the temperature over a long acquisition time ( $\sim 15$  h) which has a slope of  $-1.03 \text{ mK h}^{-1} \pm 0.03 \text{ mK h}^{-1}$ . On the right panel the orange line represents the exponential fit (eq. (7.1)) of the first temperature step. Central panels: finite element simulation for the HWP temperature. The continuous line shows the external side of the HWP that is directly in contact with the PEEK ring; the dashed line shows the temperature in the central part of the HWP. We assume the upper part of the PEEK ring has the same temperature as the aluminum bearing shown by the continuous line in the top panel. Bottom panels: the HWP position read by the absolute encoder.

the rotation system. A weighted average of the time constants obtained ( $\sim 40$  fits for 8 scans) provides the best value of  $\tau = 28.6 \text{ s} \pm 0.6 \text{ s}$ .

During rotation, eq. (7.1) becomes:

$$C \frac{d[T(t) - T_B]}{dt} = -K[T(t) - T_B] + \dot{Q}_M \quad (7.3)$$

where  $\dot{Q}_M$  is the heating power induced by the rotation. In principle this value depends on the rotation speed which is kept approximately constant during this test. The solution of the thermal equation is:

$$T(t) - T_B = C^* e^{-\frac{Kt}{C}} + \frac{\dot{Q}_M}{K} \quad (7.4)$$

The average heating caused by a single step of the rotator is  $\Delta T = 33 \pm 7 \text{ mK}$ , a small variation with respect to the equilibrium temperature. The estimated power load is  $\dot{Q}_M = 2 \pm 1.5 \text{ mW}$ , found by the fit offset and by assuming  $K = 46 \text{ mW K}^{-1}$  (see subsection 4.3.1). This value is compatible with the upper limit estimated during the nitrogen tests (section 6.1) and, if needed, the power dissipated could be reduced by lowering (via software) the speed of the rotator.

horn	distance to center [mm]	$\Delta T$ [mK]	$\Delta P$ [ $10^{-15}$ W]
central	9.9	0.04	0.08
middle	29.7	0.23	0.43
edge	69.3	1.3	2.00

**Table 2.** The effect of rotating the HWP, in terms of temperature and power gradient, for three selected horns: one placed near the center, one in the middle, and one near the edge of the HWP. The power gradient integrated over the band is also reported.

### 7.1.1 HWP temperature

In order to determine the temperature of the HWP, we set up a finite element thermal model (FEM) in COMSOL Multiphysics.<sup>7</sup> The PEEK ring which houses the HWP is heated up with the measured temperature profile (top panel of figure 7) and the thermal contact with the HWP is assumed to be perfect. The HWP was assumed to be made of polypropylene and its thermal capacity and specific heat as a function of temperature were obtained from Barucci et al. [39] and Runyan et al. [45]. We have also taken into account the radiation heat load produced by the 8.5 K filters which was absorbed by the HWP with an absorption coefficient  $\xi = 0.03$ . The middle panel of figure 7 shows the expected temperature of the HWP at its center and edge, close to the PEEK ring.

During the whole operation seen in figure 7, the maximum temperature gradient between these two points is 10 mK. The HWP is placed 82.3 mm above the system aperture stop [7] therefore, given their beam size, different horns observe different 34 mm portions of the HWP surface. We evaluated the temperature and power gradient seen by a single horn by convolving its main beam with the temperature profile obtained using the FEM simulation. In table 2 are reported the peak to peak HWP temperature variations ( $\Delta T$ ) in the spots seen by different horns, and the corresponding power variations ( $\Delta P$ ) after integration over the band pass filter in front of the detector. The power variations can be compared with the detectors NEP  $\simeq 0.1 \times 10^{-15} \text{ W}/\sqrt{\text{Hz}}$ .

In figure 8 the three horns are shown in blue (the central one), red (an edge one) and green (a middle one). The three horns represent the best, the worst, and an intermediate scenario in terms of power gradient over the aperture plane.

During the calibration phase no effect was seen on the detectors while the HWP was rotating. This was because of a neutral density filter placed after the back-to-back horn array (see section 9), which had a transmissivity of 0.09. During sky observations, we expect to see steps and settling in the detector time-ordered data and plan to filter these features by means of decorrelation from a common mode template.

## 8 Optical properties

The QUBIC polarimeter is composed of a polypropylene meta-material HWP, i.e. Pisano et al. [46], followed by a polarizer made of copper strips deposited on a mylar substrate. In the QUBIC-TD the HWP and the polarizer have a reduced diameter with respect to the FI configuration, 180 mm and 370 mm respectively. The HWP and the polarizer have been characterized with dedicated laboratory measurements by the Astronomy Instrumentation Group (AIG) in Cardiff by using a vector network analyzer (VNA). In this section we

<sup>7</sup><https://www.comsol.com>.

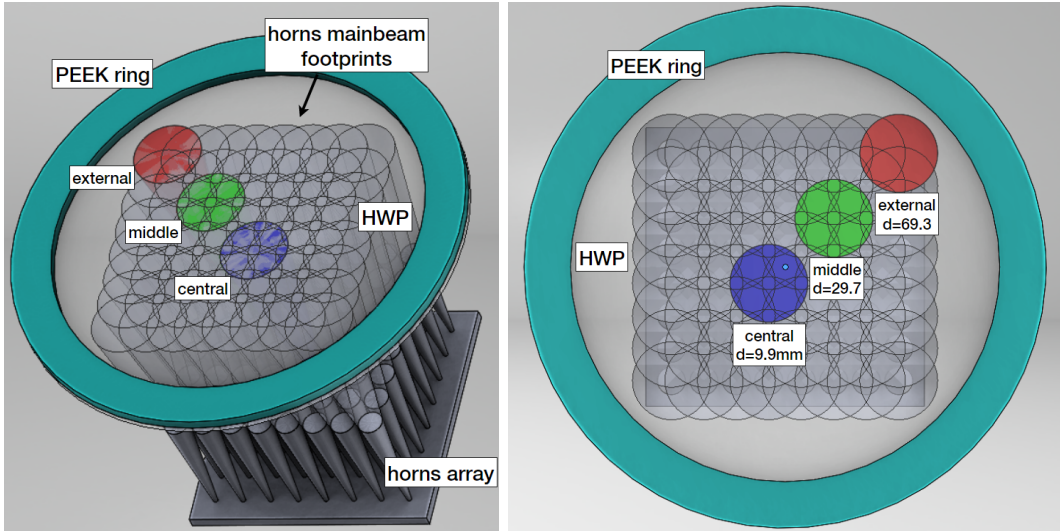


**Figure 8.** Illumination of the HWP by the horn array. The distance between the HWP and the horn apertures is 82.3 mm. The footprint of selected horns, a central, middle and edge one, are colored blue, green and red, respectively. The full width at half maximum of the beam,  $15^\circ$  [8], illuminates a disk with diameter 34 mm.

construct a model for the modulation at a single frequency of 150 GHz. This model is used in the following section to reconstruct the input Stokes vector and to evaluate the instrumental cross-polarization ( $\chi_{\text{Pol}}$ ).

### 8.1 A model for the QUBIC-TD polarimeter

We consider a VNA that illuminates a HWP with fully linearly polarized light at different frequencies. By measuring the transmitted intensity at different HWP rotation angles ( $0^\circ$ ,  $45^\circ$  and  $90^\circ$  with respect to the HWP C-axis<sup>8</sup>) we give the transmission Jones matrix at 150 GHz [47]:

$$J_{\text{HWP}} = \begin{bmatrix} 0.9584 & 9.9 \cdot 10^{-5} \\ 7.2 \cdot 10^{-5} & -0.9589 + 0.02j \end{bmatrix}.$$

The corresponding Mueller matrix can then be obtained from:

$$M_{ij} = \frac{1}{2} \text{tr}(\sigma_i \cdot J \cdot \sigma_j \cdot J^\dagger) \quad (8.1)$$

where  $\sigma_n$  ( $n = [0, \dots, 3]$ ) are Pauli matrices such as Anderson [48]. The HWP Muller matrix is:

$$M_{\text{HWP}} = \begin{bmatrix} M_{TT} & M_{TQ} & M_{TU} & M_{TV} \\ M_{TQ} & M_{QQ} & M_{QU} & M_{QV} \\ M_{TU} & M_{QU} & M_{UU} & M_{UV} \\ M_{TV} & M_{QV} & M_{UV} & M_{VV} \end{bmatrix} = \begin{bmatrix} 0.92 & -1.99 \cdot 10^{-4} & < 10^{-7} & < 10^{-6} \\ -1.99 \cdot 10^{-4} & 0.92 & 1.91 \cdot 10^{-4} & < 10^{-7} \\ < 10^{-7} & 1.91 \cdot 10^{-4} & -0.92 & -2.4 \cdot 10^{-2} \\ < 10^{-6} & < 10^{-7} & 2.4 \cdot 10^{-2} & -0.92 \end{bmatrix}.$$

The polarizer is a  $10 \mu\text{m}$  period lithographically etched copper wire device. The ‘wires’ are  $5 \mu\text{m}$  wide and  $400 \text{ nm}$  thick; the substrate is  $1.9 \mu\text{m}$ -thick mylar. The mylar optical

<sup>8</sup>The meta-material HWP is characterized by a Lerner-type geometry (described in Pisano et al. [47]) where capacitive and inductive elements are orthogonal. The C-axis is the axis parallel to the capacitive one.

parameters at 150 GHz are:  $n = 1.830 + 0.03i$ ,  $\epsilon = 3.35$ ,  $\tan \delta = 10^{-4}$ , such as Wentworth et al. [49]. The Mueller matrix, measured with a VNA, such as for the HWP at 150 GHz, for an angle of incidence of zero degrees is:

$$M_{px} = \frac{1}{2} \begin{bmatrix} P_x & P_x & 0 & 0 \\ P_x & P_x & 0 & 0 \\ 0 & 0 & 0 & 0 \\ 0 & 0 & 0 & 0 \end{bmatrix} = \frac{1}{2} \begin{bmatrix} 0.9995 & 0.9995 & 0 & 0 \\ 0.9995 & 0.9995 & 0 & 0 \\ 0 & 0 & 0 & 0 \\ 0 & 0 & 0 & 0 \end{bmatrix}.$$

We can now provide the polarimeter model for the QUBIC-TD as follows:

$$s_{\text{out}} = M_{px} \cdot M_{\text{rot}}(\theta)^{-1} \cdot M_{\text{HWP}} \cdot M_{\text{rot}}(\theta) \cdot s_{\text{in}} \quad (8.2)$$

where  $s_{\text{in}} = (T, Q, U, V)$  is the input Stokes vector and  $M_{\text{rot}}(\theta)$  represents rotation by an angle  $\theta$  with respect to the optical axis. The first component of  $s_{\text{out}}$  is the intensity at the detector, modulated by the HWP orientation  $\theta$ , see also Bryan et al. [50]:

$$\begin{aligned} I_r = & \frac{1}{2}T [M_{TQ}P_x \cos(2\theta) + M_{TT}P_x - M_{TU}P_x \sin(2\theta)] \\ & + \frac{1}{2}Q \{ [M_{QQ}P_x \cos(2\theta) - M_{QU}P_x \sin(2\theta) + M_{TQ}P_x] \cos(2\theta) \\ & - [M_{QU}P_x \cos(2\theta) + M_{TU}P_x - M_{UU}P_x \sin(2\theta)] \sin(2\theta) \} \\ & + \frac{1}{2}U \{ [M_{QQ}P_x \cos(2\theta) - M_{QU}P_x \sin(2\theta) + M_{TQ}P_x] \sin(2\theta) \\ & + [M_{QU}P_x \cos(2\theta) + M_{TU}P_x - M_{UU}P_x \sin(2\theta)] \cos(2\theta) \} \\ & + \frac{1}{2}V [M_{QV}P_x \cos(2\theta) + M_{TV}P_x - M_{UV}P_x \sin(2\theta)] \end{aligned} \quad (8.3)$$

For the purposes of this paper we neglect terms  $< 10^{-6}$  because they are expected to be below the noise level and  $\chi_{\text{Pol}}$ . The intensity at the detector becomes:

$$\begin{aligned} I_r = & I_r^d + I_r^{od} \\ = & \epsilon \cdot \frac{1}{2} [T + Q \cos(4\theta) + U \sin(4\theta)] + \frac{1}{2}P_x [T(M_{TQ} \cos(2\theta)) \\ & + Q(M_{TQ} \cos(2\theta) - M_{QU} \sin(4\theta)) + U(M_{TQ} \sin(2\theta) - M_{QU} \cos(4\theta)) \\ & - V(M_{UV} \sin(2\theta))] \end{aligned} \quad (8.4)$$

where the intensity,  $I_r$ , has been divided into two parts:  $I_r^d$ , comprising the diagonal terms of the Mueller matrix, and  $I_r^{od}$ , comprising the off-diagonal terms greater than  $10^{-6}$ . The efficiency factor  $\epsilon = M_{TT}P_x = M_{QQ}P_x = -M_{UU}P_x = -M_{VV}P_x = 0.92$ . The  $I_r^{od}$  term modulates all the  $s_{\text{in}}$  terms: by assuming no circular polarization in the laboratory we can neglect the last term of (8.4). The remaining part of  $I_r^{od}$  is always  $< 1.99 \cdot 10^{-4}$ . During the calibration phase, we used both the model in (8.3) and the term  $I_r^d$  in (8.4) to fit the data, deriving the same results.

## 9 Polarization modulation

The QUBIC polarimeter has been tested during a calibration campaign, with the focal plane cooled to 348 mK and with the HWP rotator at a temperature of 8 K. The measurements

were performed by setting the calibration source frequency to 150 GHz, where the HWP works as a  $180^\circ$  phase retarder for the two orthogonal polarizations to within  $10^{-4}$ , as shown in section 8.1.

The calibration source consists of a 10 GHz synthesizer followed by two multipliers that increase the operating frequency into the 130-170 GHz band (*VDI electronics*). The source waveguide is coupled to a conical corrugated horn using a rectangular-to-circular transition and is linearly polarized with cross polarization and return loss  $< -30$  dB, such as in Mandelli et al. [51]. It is modulated at 1 Hz. Although originally developed to work at a distance of 40 m for the FI calibration at the observing site in Argentina, the source was placed 11 m away from the QUBIC cryostat in the laboratory in APC, Paris, for these calibration tests. Because of this, the measured signal amplitude during the calibration phase was more than one order of magnitude higher, resulting in non-linear effects and, in some cases, saturation of the signal read by the TES detectors. To dampen the source signal, a neutral density filter ( $\sim 9\%$  transmissivity) was placed directly after the back-to-back horn array. Nevertheless, a non-linear correction must be applied to some of the data (see below).

Here we report results from data acquired by the TES detectors, providing polarization parameters and cumulative distributions of  $\chi_{\text{Pol}}$  estimates from TESs with signal-to-noise ratio,  $S/N > 5$ .

The time ordered data (TOD) acquired at the seven nominal rotator positions were first processed using Fourier transforms to calculate power spectra. An exponential fit, applied to the spectra but excluding the main peak from the 1 Hz modulated input source, was used to estimate the noise level of each acquisition by integrating over the main band [0.7, 1.3] Hz. We show in the right panel of figure 9 how the exponential model best fits the acquisition at the 3rd HWP position, where the signal is at the minimum of the polarization modulation curve and only the noise contribution is present in the data. Finally, the noise contribution to the signal was subtracted and used as the uncertainty in the estimated signal. The power spectrum of each TOD is reported in the left panel of figure 9 with a different color for each HWP position. In figure 10 we show the final polarization modulation curve estimated with the procedure described here. Curves from four representative TESs at different locations on the focal plane are reported. In the same figure, the fit to the data is shown in red. The fit has been performed with the function:

$$I = \epsilon \cdot \frac{1}{2} [T + Q \cos(4\theta + \phi)] \quad (9.1)$$

where pure linearly polarized light is assumed as input, but with a still unknown polarization angle, determined by the experimental setup alignment. An offset on the HWP orientation,  $\phi$ , is included in the fit model, providing an equivalent model to eq. (2.1). The detector response can be included in the fit model in order to treat deviations from the sinusoidal polarization modulation curve, especially for the estimates of the signals near the peak of the curve, where the input power is large. To include the detector response, we consider the model:

$$I' = k \cdot \tanh(I/k) \quad (9.2)$$

which grows linearly with the signal in the limit  $I \ll k$  and tends to  $k$  for  $I \gg k$ , where  $I$  is the modulated intensity of eq. (9.1) and  $k$  is the saturation parameter. Measurements of the TES linearity were only performed when the polarimeter was not yet assembled within the QUBIC cryostat, and therefore cannot be included in the data analysis process. Linearity measurements will be performed again with the inclusion of the half-wave plate polarimeter.

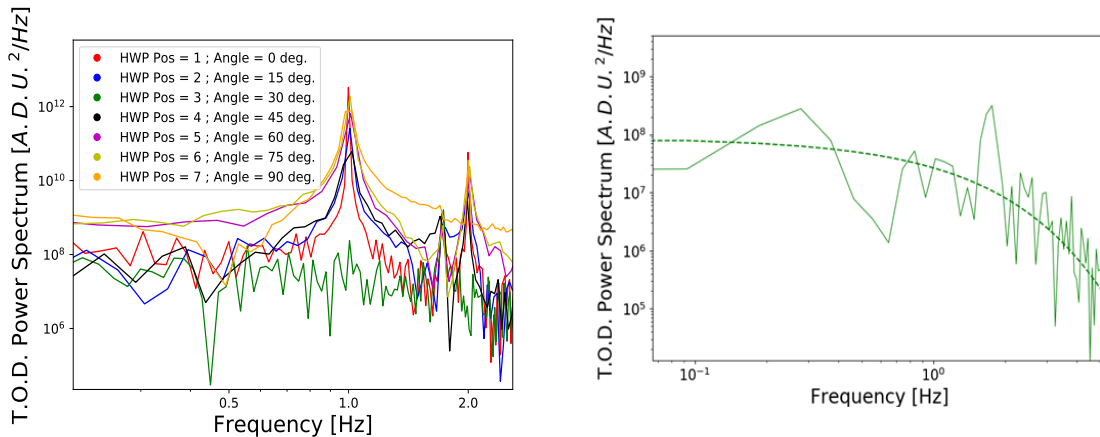


**Figure 9.** Left: power spectra of the TOD in arbitrary digital units at each HWP position, shown using different colors. The spectra at the 3<sup>rd</sup> HWP position correspond to data close to the minimum of the polarization modulation curve and are therefore dominated by the noise. Right: power spectrum of TOD acquired at the 3<sup>rd</sup> HWP position; the dashed line shows the exponential fit to the data used for the noise estimation. The calibration source signal emits at 1 Hz as expected, at about 1.7 Hz the pulse tube signal can be seen in the spectra as a vibration effect on the detectors, and a lower amplitude calibration source harmonic can be seen at 2 Hz.

We use the eq. (9.1) and (9.2) to model the measured counts as a function of  $\theta$ , fitting  $T$ ,  $Q$  and  $\phi$  for the linear model, and fitting also the  $k$  parameter for the non-linear model. In figure 10 we show the best fit of the two models: the linear TES response (red continuous line) and the non-linear TES response (blue continuous line). The bottom panels show how the non-linear model best fits the data collected by non-linear detectors, while it provides an equivalent model in comparison with the linear model when the detector shows a linear response (top-left panel).

### 9.1 $\chi$ -polarization

To compute the cross polarization, we follow the definition given by eq. (1) in Ludwig et al. [52], in which a rectangular coordinate system is defined, where one unit vector is taken as the direction of the reference polarization, and another as the direction of cross polarization. Hence, if  $\vec{E}$  is the incoming electric field, the reference polarization component of  $\vec{E}$  is  $E \cdot \hat{i}_{\text{ref}}$  and the cross polarization component of  $\vec{E}$  is  $E \cdot \hat{i}_{\text{cross}}$ .

We can write equation (2.1):

$$I_{\text{max}} = I(\theta') = \epsilon \cdot \frac{1}{2} [T + Q \cos(4\theta')]. \quad (9.3)$$

For a fully polarized source, along  $\hat{i}_{\text{ref}}$ , and for an ideal polarimeter  $I_{\text{max}}$  should equal to  $T$  because all the radiation is transmitted by the polarizer. We can rewrite equation (9.3) in terms of the polarization efficiency  $\epsilon_P = Q/T$ :

$$I_{\text{max}} = I(\theta') = \epsilon \cdot \frac{T}{2} [1 + \epsilon_P \cos(4\theta')]. \quad (9.4)$$

Assuming both the incoming radiation and the polarizer transmission axis along  $\hat{i}_{\text{ref}}$ ,  $\theta'$  is the HWP angle when occurs the maximum of intensity,  $I_{\text{max}}$ . Instead:

$$I_{\text{min}} = I(\theta'') = \epsilon \cdot \frac{1}{2} [T + Q \cos(4\theta'')], \quad (9.5)$$

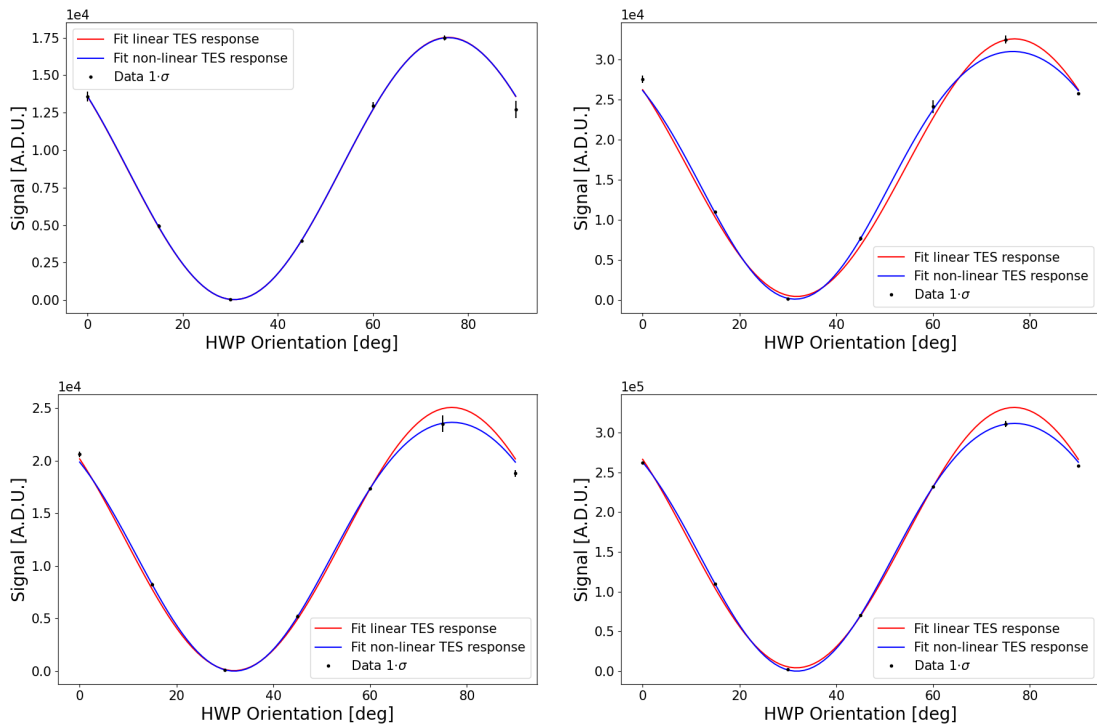


**Figure 10.** Polarization modulation curves acquired at the nominal HWP positions  $[0^\circ, 15^\circ, 30^\circ, 45^\circ, 60^\circ, 75^\circ, 90^\circ]$ , for four TES detectors at different locations in the focal plane and given in arbitrary digital units. These are representative cases. Data points are estimated via integration of the TOD Fourier transform over the band  $[0.7, 1.3]$  Hz at each nominal HWP position. Two models are used to fit the data: a model as in eq. (9.1) (red line) and a model where the response of the detector is included as a function which deviates from linearity for high input power, as in eq. (9.2) (blue line).

where  $\theta''$  is the HWP angle when the minimum of the intensity,  $I_{\min}$ , occurs. In this case the HWP rotates the incoming radiation along  $\hat{i}_{\text{cross}}$ , so it is reflected by the polarizer. The following relation holds for  $\theta'$  and  $\theta''$ :

$$\theta' = \theta'' + \frac{\pi}{4} \quad (9.6)$$

For a fully polarized source, along  $\hat{i}_{\text{ref}}$ , and for an ideal polarimeter,  $I_{\min}$  should be equal to zero because all the radiation is reflected by the polarizer. The radiation transmitted by the polarizer when the HWP angle is  $\theta''$  is along  $\hat{i}_{\text{cross}}$ . We can rewrite equation (9.5):

$$I_{\min} = I(\theta'') = \epsilon \cdot \frac{T}{2} \left[ 1 + \epsilon_P \cos(4\theta'') + \chi_{\text{Pol}} \cos(4\theta'') \right], \quad (9.7)$$

where  $\chi_{\text{Pol}}$  is the cross-polarization. We use the eq. (9.1) and (9.2) to model the measured counts as a function of  $\theta$ , fitting  $T$ ,  $Q$ , and  $\phi$  for the linear model, adding to the fit also the  $k$  parameter for the non-linear model. The angle  $\theta''$  is found where the minimum of the model, used to fit the data, occurs. The  $\chi_{\text{Pol}}$  is obtained from eq. (9.7). We prefer to retrieve  $\theta''$  from the model and not fitting the data because of the low resolution of data in terms of  $\theta$ . The efficiency factor  $\epsilon$  is provided by the independent laboratory characterization shown in

TES #	Linear TES Response				Non-Linear TES Response			
	$T \cdot 10^4$ [A.D.U.]	$\epsilon_P$	$\chi_{Pol}$ [%]	PTE $P_{\chi^2}$	$T \cdot 10^4$ [A.D.U.]	$\epsilon_P$	$\chi_{Pol}$ [%]	PTE $P_{\chi^2}$
95	$3.7 \pm 0.2$	$0.92 \pm 0.07$	$4.1^{+2.9}_{-1.3}$	0.12	$5.2 \pm 0.4$	$1.02 \pm 0.12$	$0.16^{+0.26}_{-0.37}$	0.77
13	$34.9 \pm 0.7$	$0.99 \pm 0.04$	$0.5^{+1.2}_{-0.6}$	0.60	$49.1 \pm 5.0$	$1.03 \pm 0.15$	$0.01^{+0.16}_{-0.00}$	0.76
23	$22.9 \pm 0.4$	$1.06 \pm 0.03$	$0.41^{+0.23}_{-0.14}$	0.14	$26.4 \pm 1.0$	$0.99 \pm 0.05$	$0.10^{+0.12}_{-0.11}$	0.86
54	$25.4 \pm 0.8$	$0.81 \pm 0.06$	$8.7^{+7.8}_{-1.0}$	0.02	$43.1 \pm 2.6$	$0.99 \pm 0.08$	$0.48^{+0.13}_{-0.43}$	0.99
63	$55.0 \pm 1.0$	$0.98 \pm 0.03$	$0.69^{+0.08}_{-0.62}$	0.35	$37.7 \pm 0.6$	$1.00 \pm 0.03$	$0.06^{+0.07}_{-0.07}$	0.98
98	$48.2 \pm 0.6$	$0.98 \pm 0.02$	$0.4^{+1.5}_{-0.5}$	0.19	$70.5 \pm 0.4$	$1.00 \pm 0.01$	$0.01^{+0.39}_{-0.08}$	0.99
99	$37.3 \pm 0.3$	$1.03 \pm 0.02$	$0.11^{+0.42}_{-0.05}$	0.86	$37.3 \pm 0.3$	$1.03 \pm 0.02$	$0.11^{+0.14}_{-0.15}$	0.86
159	$12.5 \pm 0.2$	$0.81 \pm 0.02$	$0.03^{+0.29}_{-0.31}$	0.41	$15.6 \pm 0.4$	$1.00 \pm 0.04$	$0.00^{+0.15}_{-0.02}$	0.54
170	$67.0 \pm 0.7$	$0.97 \pm 0.02$	$1.12^{+0.93}_{-0.24}$	0.20	$21.2 \pm 0.4$	$1.00 \pm 0.03$	$0.1^{+1.9}_{-0.2}$	0.45
175	$26.9 \pm 0.8$	$1.07 \pm 0.05$	$0.29^{+0.30}_{-0.01}$	0.74	$26.9 \pm 0.8$	$1.07 \pm 0.05$	$0.29^{+0.31}_{-0.01}$	0.74
238	$27.7 \pm 0.8$	$1.03 \pm 0.04$	$0.07^{+0.02}_{-0.02}$	0.28	$27.7 \pm 0.9$	$1.03 \pm 0.05$	$0.07^{+0.23}_{-0.15}$	0.28

**Table 3.** Results from TES#95, close to the center of the focal plane, and from other detectors as representative cases. TESs #95, 54, 63, 98 show non-linear behaviour, as illustrated by the improved PTE when the non-linear detector response is included in the model.

section 8.1. Although  $\epsilon$  is an overall multiplicative factor, and therefore it is not critical for the final results.

## 9.2 Results

In this section we report the measured polarization parameters  $T$ ,  $Q$ ,  $\epsilon_P$ , together with the estimate of the cross polarization and the  $\chi^2$  probability-to-exceed (PTE) estimate between data and models. The best fit parameters in table 3 show a polarization efficiency close to 99%.

When a non-linear detector response is included in the model, 38% of TESs show reduced  $\chi^2$  values that show reduction in value toward 1, with variations  $> 10\%$ , and 28% of TES detectors show output polarization parameters closer to the pure linear polarization state, as expected for the signal produced by the calibration source, and reduced  $\chi_{Pol}$  estimates. The results obtained from the remaining detectors show no differences in the estimated polarization parameters within  $1\sigma$  between the two models, showing practically the same PTE values.

We report in table 3, as an example from the TES detectors selected, the results for the TES closest to the center of the focal plane (#95). Results of the most representative cases are also reported in the table. When the non-linear detector response is included, TESs #95, 54, 63, 98 show improved PTE,  $\epsilon_P$  estimates close to unity, with tighter constraints and deviations from unity  $< 1\%$ , and reduced  $\chi_{pol}$  estimates. TES # 13, 23, 159, 170 show an improved PTE and reduced  $\chi_{pol}$  estimates when the non-linearity is included, while the  $\epsilon_P$  estimates are similar between the models. TES bolometers #99, 175, 238 show compatible results within  $1\sigma$  between the two models over all the estimated polarization parameters.

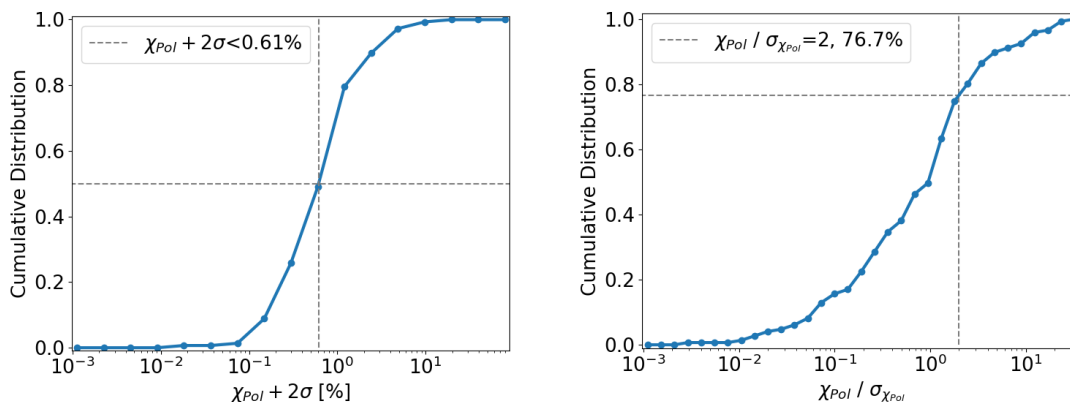


**Figure 11.** Left: cumulative distribution of  $\chi_{\text{Pol}} + 2\sigma$ , the dashed gray lines indicate the median value; right:  $\chi_{\text{Pol}}/\sigma_{\chi_{\text{Pol}}}$  cumulative distribution, the dashed gray lines indicate the  $\chi_{\text{Pol}} + 2\sigma$  value; both cumulative distributions are produced by considering a non-linear TES response in the model.

What is summarized in table 3 shows how the non-linear model helps in recovering the information from non-linear TESs, also producing no bias on linear detectors. Below we show the estimates of  $\epsilon_P$  and  $\chi_{\text{Pol}}$  from the non-linear model only.

The median deviation of  $\epsilon_P$  from unity is  $< 1.8\%$  when non-linearity is included in the model. The polarization efficiency for the detectors with the best signal-to-noise ratio ( $S/N > 5$ ) is always  $> 99\%$  (68% C.L.), TES #98 in table 3 is a representative case. The smallest 95% C.L. upper-limit on  $\chi_{\text{Pol}}$  over all TESs is 0.05% with a  $PTE = 0.96$ . The cumulative distribution of the  $\chi_{\text{Pol}}$  estimates provides a median value of 0.12%. The cumulative distribution of the  $\chi_{\text{Pol}} + 2\sigma$  upper-limit is reported in figure 11 (Left) together with the cumulative distribution of the ratio  $\chi_{\text{Pol}}/\sigma_{\chi_{\text{Pol}}}$  (Right). The median value of the  $\chi_{\text{Pol}} + 2\sigma$  cumulative distribution is 0.61%. Given the S/N of these measurements, figure 11 (Right) shows that 77% of detectors have a  $\chi_{\text{Pol}}$  compatible with zero within  $2\sigma$  and figure 11 (Left) shows that 71% of detectors have a  $\chi_{\text{Pol}} + 2\sigma$  upper-limit  $< 1\%$ .

There is no evidence of dependence between  $\chi_{\text{Pol}}$  and the pixel position on the focal plane. This is consistent with the optical scheme of QUBIC, see [7]. After the QUBIC Stokes polarimeter, incoming radiation produces an interferogram on the focal plane after separation by the horn array and beam combining by the two mirrors. As a result, any incoherent radiation, such as might be produced by multiple reflections, is effectively filtered out.

## 10 Conclusions

We have developed a polarimeter for the CMB B-mode QUBIC experiment that operates at cryogenic temperatures. The polarimeter, composed of a step-by-step rotating meta-material-HWP, was tested at room temperature, in liquid nitrogen, and within the QUBIC cryostat. A custom-made position readout system has been developed and tested, allowing the HWP to be moved and controlled with a precision of  $0.15^\circ$ . In this paper we have shown how the device will allow us to carry out CMB measurements by limiting the heating of the HWP to values  $\leq 10$  mK. The HWP has been rotated at a speed of  $7.5^\circ/\text{s}$  to its seven nominal positions, with no data-loss and no cryogenic issues detected on the 4K stage. We estimate  $< 5.0$  mW (95% C.L.) dissipated on the cryogenic stage during operation, satisfying the low temperature requirement.

We also report on 150 GHz polarization measurements that demonstrate our ability to reconstruct the input Stokes vector of purely polarized input light, with a polarization efficiency  $> 99\%$  (68% C.L.). We determined a median value of the  $\chi_{\text{Pol}}$  cumulative distribution of 0.12%, and of the  $\chi_{\text{Pol}} + 2\sigma$  cumulative distribution  $< 0.61\%$ . Given the S/N of this measurement, 71% of detectors have a  $\chi_{\text{Pol}} + 2\sigma$  upper limit  $< 1\%$  and 77% of detectors show a  $\chi_{\text{Pol}}$  compatible with zero within  $2\sigma$ , when the non-linearity of the detector induced by the calibration source is included.

The measured optical model of the QUBIC polarimeter, in the form of Mueller matrices, is reported here at 150 GHz and will be included in future work to describe the performance of the QUBIC polarimeter. The QUBIC HWP rotator satisfies all the requirements imposed by the scanning strategy and thermal budget of the experiment.

## Acknowledgments

QUBIC is funded by the following agencies. France: ANR (Agence Nationale de la Recherche) 2012 and 2014, DIM-ACAV (Domaine d'Interet Majeur-Astronomie et Conditions d'Apparition de la Vie), CNRS/IN2P3 (Centre national de la recherche scientifique/Institut national de physique nucléaire et de physique des particules), CNRS/INSU (Centre national de la recherche scientifique/Institut national 8 Battistelli et al. de sciences de l'univers). Italy: CNR/PNRA (Consiglio Nazionale delle Ricerche/Programma Nazionale Ricerche in Antartide) until 2016, INFN (Istituto Nazionale di Fisica Nucleare) since 2017. Argentina: MINCyT (Ministerio de Ciencia, Tecnología e Innovación), CNEA (Comisión Nacional de Energía Atómica), CONICET (Consejo Nacional de Investigaciones Científicas y Técnicas).

D. Burke and J.D. Murphy acknowledge funding from the Irish Research Council under the Government of Ireland Postgraduate Scholarship Scheme. D. Gayer and S. Scully acknowledge funding from the National University of Ireland, Maynooth. D. Bennett acknowledges funding from Science Foundation Ireland.

## References

- [1] QUBIC collaboration, *QUBIC I: Overview and science program*, *JCAP* **04** (2022) 034 [[arXiv:2011.02213](#)] [[INSPIRE](#)].
- [2] BICEP and KECK collaborations, *Improved Constraints on Primordial Gravitational Waves using Planck, WMAP, and BICEP/Keck Observations through the 2018 Observing Season*, *Phys. Rev. Lett.* **127** (2021) 151301 [[arXiv:2110.00483](#)] [[INSPIRE](#)].
- [3] A. Tartari et al., *QUBIC: A Fizeau Interferometer Targeting Primordial B-Modes*, *J. Low Temp. Phys.* **184** (2016) 739 [[INSPIRE](#)].
- [4] M. Piat et al., *QUBIC: the Q&U Bolometric Interferometer for Cosmology*, *J. Low Temp. Phys.* **167** (2012) 872 [[INSPIRE](#)].
- [5] QUBIC collaboration, *QUBIC II: Spectro-polarimetry with bolometric interferometry*, *JCAP* **04** (2022) 035 [[arXiv:2010.15119](#)] [[INSPIRE](#)].
- [6] L. Mele et al., *The QUBIC instrument for CMB polarization measurements*, in *J. Phys. Conf. Ser.* **1548** (2020) 012016.
- [7] QUBIC collaboration, *QUBIC VIII: Optical design and performance*, *JCAP* **04** (2022) 041 [[arXiv:2008.10119](#)] [[INSPIRE](#)].
- [8] QUBIC collaboration, *QUBIC VII: The feedhorn-switch system of the technological demonstrator*, *JCAP* **04** (2022) 040 [[arXiv:2008.12721](#)] [[INSPIRE](#)].

- [9] M.A. Bigot-Sazy, R. Charlassier, J.C. Hamilton, J. Kaplan and G. Zahariade, *Self-calibration: an efficient method to control systematic effects in bolometric interferometry*, *Astron. Astrophys.* **550** (2013) A59 [[arXiv:1209.4905](#)] [[INSPIRE](#)].
- [10] QUBIC collaboration, *QUBIC IV: Performance of TES bolometers and readout electronics*, *JCAP* **04** (2022) 037 [[arXiv:2101.06787](#)] [[INSPIRE](#)].
- [11] BICEP2 collaboration, *Detection of B-Mode Polarization at Degree Angular Scales by BICEP2*, *Phys. Rev. Lett.* **112** (2014) 241101 [[arXiv:1403.3985](#)] [[INSPIRE](#)].
- [12] A. Kogut et al., *The Primordial Inflation Explorer (PIXIE): A Nulling Polarimeter for Cosmic Microwave Background Observations*, *JCAP* **07** (2011) 025 [[arXiv:1105.2044](#)] [[INSPIRE](#)].
- [13] D.H. Goldstein, *Polarized Light 3th edition*, CRC Press (2011).
- [14] B.R. Johnson et al., *MAXIPOL: Cosmic Microwave Background Polarimetry Using a Rotating Half-Wave Plate*, *Astrophys. J.* **665** (2007) 42 [[astro-ph/0611394](#)] [[INSPIRE](#)].
- [15] EBEX collaboration, *The EBEX Balloon-borne Experiment — Detectors and Readout*, *Astrophys. J. Suppl.* **239** (2018) 8 [[arXiv:1803.01018](#)] [[INSPIRE](#)].
- [16] C.J. MacTavish et al., *Spider Optimization: Probing the Systematics of a Large Scale B-Mode Experiment*, *Astrophys. J.* **689** (2008) 655 [[arXiv:0710.0375](#)] [[INSPIRE](#)].
- [17] P. de Bernardis et al., *SWIPE: a bolometric polarimeter for the Large-Scale Polarization Explorer*, *Proc. SPIE Int. Soc. Opt. Eng.* **8452** (2012) 3F [[arXiv:1208.0282](#)] [[INSPIRE](#)].
- [18] L. Lamagna et al., *Progress report on the Large Scale Polarization Explorer*, [arXiv:2005.01187](#) [[INSPIRE](#)].
- [19] S.W. Henderson et al., *Advanced ACTPol Cryogenic Detector Arrays and Readout*, *J. Low Temp. Phys.* **184** (2016) 772 [[arXiv:1510.02809](#)] [[INSPIRE](#)].
- [20] QUBIC collaboration, *QUBIC III: Laboratory characterization*, *JCAP* **04** (2022) 036 [[arXiv:2008.10056](#)].
- [21] EBEX collaboration, *The EBEX Balloon-borne Experiment — Optics, Receiver, and Polarimetry*, *Astrophys. J. Suppl.* **239** (2018) 7 [[arXiv:1703.03847](#)] [[INSPIRE](#)].
- [22] ABS collaboration, *Modulation of cosmic microwave background polarization with a warm rapidly rotating half-wave plate on the Atacama B-Mode Search instrument*, *Rev. Sci. Instrum.* **85** (2014) 024501 [[arXiv:1310.3711](#)] [[INSPIRE](#)].
- [23] A. Ritacco et al., *Polarimetry at millimeter wavelengths with the NIKA camera: calibration and performance*, *Astron. Astrophys.* **599** (2017) A34 [[arXiv:1609.02042](#)] [[INSPIRE](#)].
- [24] A. Ritacco et al., *Observing with NIKA2Pol from the IRAM 30m telescope: Early results on the commissioning phase*, *EPJ Web Conf.* **228** (2020) 00022 [[arXiv:1912.07894](#)] [[INSPIRE](#)].
- [25] B.P. Crill et al., *SPIDER: A Balloon-borne Large-scale CMB Polarimeter*, *Proc. SPIE Int. Soc. Opt. Eng.* **7010** (2008) 70102P [[arXiv:0807.1548](#)] [[INSPIRE](#)].
- [26] M. Salatino, P. de Bernardis and S. Masi, *A cryogenic waveplate rotator for polarimetry at mm and sub-mm wavelengths*, *Astron. Astrophys.* **528** (2011) A138 [[arXiv:1006.5392](#)] [[INSPIRE](#)].
- [27] L. Moncelsi et al., *Empirical modelling of the BLASTPol achromatic half-wave plate for precision submillimetre polarimetry*, *Mon. Not. Roy. Astron. Soc.* **437** (2014) 2772 [[arXiv:1208.4866](#)] [[INSPIRE](#)].
- [28] S. Takakura et al., *Performance of a continuously rotating half-wave plate on the POLARBEAR telescope*, *JCAP* **05** (2017) 008 [[arXiv:1702.07111](#)] [[INSPIRE](#)].
- [29] C.A. Hill et al., *A cryogenic continuously rotating half-wave plate for the POLARBEAR-2b cosmic microwave background receiver*, *Rev. Sci. Instrum.* **91** (2020) 124503 [[arXiv:2009.03972](#)] [[INSPIRE](#)].

- [30] G. Pisano et al., *Development and application of metamaterial-based Half-Wave Plates for the NIKA and NIKA2 polarimeters*, *Astron. Astrophys.* **658** (2022) [[arXiv:2006.12081](#)] [[INSPIRE](#)].
- [31] B.R. Johnson et al., *A large-diameter hollow-shaft cryogenic motor based on a superconducting magnetic bearing for millimeter-wave polarimetry*, *Rev. Sci. Instrum.* **88** (2017) 105102 [[arXiv:1706.05963](#)] [[INSPIRE](#)].
- [32] A. Buzzelli, P. de Bernardis, S. Masi, N. Vittorio and G. de Gasperis, *Optimal strategy for polarization modulation in the LSPE-SWIPE experiment*, *Astron. Astrophys.* **609** (2018) A52 [[arXiv:1709.04842](#)] [[INSPIRE](#)].
- [33] J. Aumont, J.F. Macías-Pérez, A. Ritacco, N. Ponthieu and A. Mangilli, *Absolute calibration of the polarisation angle for future CMB B-mode experiments from current and future measurements of the Crab nebula*, *Astron. Astrophys.* **634** (2020) A100 [[arXiv:1805.10475](#)] [[INSPIRE](#)].
- [34] L. Pagano et al., *CMB Polarization Systematics, Cosmological Birefringence and the Gravitational Waves Background*, *Phys. Rev. D* **80** (2009) 043522 [[arXiv:0905.1651](#)] [[INSPIRE](#)].
- [35] QUBIC collaboration, *QUBIC V: Cryogenic system design and performance*, *JCAP* **04** (2022) 038 [[arXiv:2008.10659](#)] [[INSPIRE](#)].
- [36] Y. Sakurai et al., *Development of a contact-less cryogenic rotation mechanism employed for a polarization modulator unit in cosmic microwave background polarization experiments*, in *J. Phys. Conf. Ser.* **1293** (2019) 012083.
- [37] LITEBIRD JOINT STUDY GROUP collaboration, *A polarization modulator unit for the mid- and high-frequency telescopes of the LiteBIRD mission*, *Proc. SPIE Int. Soc. Opt. Eng.* **11443** (2020) 114436Z [[arXiv:2101.05188](#)] [[INSPIRE](#)].
- [38] G. D'Alessandro et al., *Ultra High Molecular Weight Polyethylene: optical features at millimeter wavelengths*, *Infrared Phys. Tech.* **90** (2018) 59 [[arXiv:1803.05228](#)] [[INSPIRE](#)].
- [39] M. Barucci, E. Gottardi, E. Olivieri, E. Pasca, L. Risegari and G. Ventura, *Low-temperature thermal properties of polypropylene*, *Cryogenics* **42** (2002) 551.
- [40] C. Barth, *High Temperature Superconductor Cable Concepts for Fusion Magnets*, KIT Scientific Publishing (2013).
- [41] G. D'Alessandro et al., *Systematic effects induced by half-wave plate precession into measurements of the cosmic microwave background polarization*, *Astron. Astrophys.* **627** (2019) A160 [[arXiv:1906.07010](#)] [[INSPIRE](#)].
- [42] P. Duthil, *Material Properties at Low Temperature*, in *CERN Accelerator School: Course on Superconductivity for Accelerators*, (2014), DOI [[arXiv:1501.07100](#)] [[INSPIRE](#)].
- [43] F. Columbro et al., *The short wavelength instrument for the polarization explorer balloon-borne experiment: Polarization modulation issues*, *Astron. Nachr.* **340** (2019) 83 [[arXiv:1904.01891](#)] [[INSPIRE](#)].
- [44] P. de Bernardis, F. Columbro, S. Masi, A. Paiella and G. Romeo, *A simple method to measure the temperature and levitation height of devices rotating at cryogenic temperatures*, *Rev. Sci. Instrum.* **91** (2020) 045118 [[INSPIRE](#)].
- [45] M.C. Runyan and W.C. Jones, *Thermal Conductivity of Thermally-Isolating Polymeric and Composite Structural Support Materials Between 0.3 and 4 K*, *Cryogenics* **48** (2008) 448 [[arXiv:0806.1921](#)] [[INSPIRE](#)].
- [46] G. Pisano, G. Savini, P.A.R. Ade and V. Haynes, *Metal-mesh achromatic half-wave plate for use at submillimeter wavelengths*, *Appl. Opt.* **47** (2008) 6251.
- [47] G. Pisano, M. Ng, V. Haynes and B. Maffei, *A broadband metal-mesh half-wave plate for millimetre wave linear polarisation rotation*, *PIER M* **25** (2012).

- [48] D.G.M. Anderson and R. Barakat, *Necessary and sufficient conditions for a mueller matrix to be derivable from a jones matrix*, *J. Opt. Soc. Am. A* **11** (1994) 2305.
- [49] F.L. Wentworth, J.C. Wiltse and F. Sobel, *Quasi-optical surface waveguide and other components for the 100- to 300-gc region*, *IRE Trans. Microwave Theory Tech.* **9** (1961) 512.
- [50] S.A. Bryan, T.E. Montroy and J.E. Ruhl, *Modeling dielectric half-wave plates for cosmic microwave background polarimetry using a mueller matrix formalism*, *Appl. Opt.* **49** (2010) 6313.
- [51] S. Mandelli et al., *A chemically etched corrugated feedhorn array for D-band CMB observations*, *Exper. Astron.* **51** (2021) 249 [[arXiv:2006.14889](https://arxiv.org/abs/2006.14889)] [INSPIRE].
- [52] A. Ludwig, *The definition of cross polarization*, *IEEE Trans. Antennas Propagat.* **21** (1973) 116.